FABRICATION AND CHARACTERIZATION OF AMORPHOUS SILICON MICROCAVITIES

A THESIS
SUBMITTED TO THE DEPARTMENT OF PHYSICS
AND THE INSTITUTE OF ENGINEERING AND SCIENCE
OF BILKENT UNIVERSITY
IN PARTIAL FULFILLMENT OF THE REQUIREMENTS
FOR THE DEGREE OF
MASTER OF SCIENCE

By
Selim TANRISEVEN
July 1999

FABRICATION AND CHARACTERIZATION OF AMORPHOUS SILICON MICROCAVITIES

A THESIS

SUBMITTED TO THE DEPARTMENT OF PHYSICS

AND THE INSTITUTE OF ENGINEERING AND SCIENCE

OF BILKENT UNIVERSITY

IN PARTIAL FULFILLMENT OF THE REQUIREMENTS

FOR THE DEGREE OF

MASTER OF SCIENCE

By

Selim TANRISEVEN

JULY 1999

I certify that I have read this thesis and that in my opinion it is fully adequate, in scope and in quality, as a dissertation for the degree of Master of Science.

Asst. Prof. Ali Serpengüzel (Supervisor)

I certify that I have read this thesis and that in my opinion it is fully adequate, in scope and in quality, as a dissertation for the degree of Master of Science.

Assoc. Prof. Ekmel Özbay

I certify that I have read this thesis and that in my opinion it is fully adequate, in scope and in quality, as a dissertation for the degree of Master of Science.

Prof. Çiğdem Erçelebi

Approved for the Institute of Engineering and Science:

Prof. Mehmet Baray,
Director of Institute of Engineering and Science

Abstract

FABRICATION AND CHARACTERIZATION OF AMORPHOUS SILICON MICROCAVITIES

Selim TANRISEVEN

M. S. in Physics

Supervisor: Asst. Prof. Ali Serpengüzel

JULY 1999

In this thesis, planar amorphous silicon microcavities were fabricated and characterized at room temperature.

Microcavities were realized by embedding the active amorphous silicon layer between distributed Bragg reflectors, which are composed of alternating silicon oxide and silicon nitride layers. All of the layers were grown by plasma enhanced chemical vapor deposition on silicon substrates. By tuning the cavity mode to emission maximum of amorphous silicon, a narrow and enhanced emission line is obtained.

Device characterization was done by means of photoluminescence, and reflectance measurements. The experimental results compare favorably with the theoretical calculations performed by transfer matrix method.

Keywords: Microcavity, Distributed Bragg Reflector, Thin Film, Fabry-Perot, Quality Factor, Resonance, Photoluminescence, Reflectance, Transfer Matrix Method, Photonics, Optoelectronics

Özet

AMORF SİLİKON MİKROÇINLAÇLARININ ÜRETİMİ VE KARAKTERİZASYONU

Selim TANRISEVEN
Fizik Yüksek Lisans
Tez Yöneticisi: Y. Doç. Dr. Ali Serpengüzel
Temmuz 1999

Bu tez çalışmasında bir boyutlu amorf silikon mikroçınlaçlar üretildi, ve oda sıcaklığında karakterize edildi.

Mikroçınlaçlar, aktif amorf silikon tabakasının, dönüşümlü silikon nitrat ve silikon oksit tabakalarından oluşan, çok katmanlı dağıtılmış Bragg yansıtıcılarının arasına yerleştirilmesiyle gerçekleştirildi. Bütün tabakalar plazma yardımlı kimyasal buhar çökeltme yöntemi ile silikon üzerine büyütüldü. Çınlaç kipinin amorf silikonun maksimum ışıma dalgaboyuna ayarlanmasıyla daha dar ve kuvvetlenmiş fotoışıma elde edildi.

Aygıtların incelenmesi, fotoışıma ve yansıma ölçümleri ile yapıldı. Deneysel sonuçların transfer matris metoduyla hesaplanan kuramsal sonuçlarla iyi bir uyum içinde olduğu görüldü..

Anahtar sözcükler: Mikroçınlaç, Dağıtılmış Bragg Yansıtıcısı, İnce Film, Fabry-Perot, Kalite Faktörü, Çınlama, Fotoışıma, Yansıma, Transfer Matris Metodu, Fotonik, Optoelektronik

Acknowledgement

I would like to express my gratitude to my supervisor Asst. Prof. Ali Serpengüzel for his guidance in this research.

I would also like to thank Alpan Bek for his help in characterization and for fruitful discussions, our good, old process engineer Murat Güre for his help in fabrication and for SEM pictures, İbrahim Kimukin for the user-friendly program, and my friends; my homemate Özgür Çakır, ODTU graduates Emre Tepedelenlioğlu, Feridun, İsa and Can for their support, and hospitality, and Ahmet İlhan Çalıkoğlu for the key.

Contents

List of Figures

List of Tables

Chapter 1

Introduction

Optical resonators with dimensions of the order of an optical wavelength can now be fabricated in a variety of solid state systems including semiconductors, organic materials, and glasses.[1] Ideally, one can isolate a single mode of the optical field in a cube a half-wavelength on a side with perfectly reflecting walls. Liquid droplets, polymer spheres, and semiconductor Fabry-Perot microcavities with dielectric mirrors are examples of microcavities with which one can approach this ideal limit and nearly isolate a few modes of the electromagnetic limit from the continuum of surrounding free-space modes.

The simplest approach to fabricating an optical microcavity is to shrink the spacing between the mirrors of a Fabry-Perot resonator to $\lambda/2n$. This structure provides a single dominant longitudinal mode that radiates into a narrow range of angles around the cavity axis.

The interaction of optically active material with isolated modes in the cavity offers interesting physical systems for basic studies and a rich variety of possible applications. Interactions between atoms and low-loss optical and microwave cavities have led to demonstrations of cavity quantum electrodynamic effects, including coupled atom-cavity modes, quantum revivals, single-atom masers and enhanced or inhibited spontaneous emission.

Microcavity resonators have the potential to provide low-cost, efficient and high-density optoelectronic light sources over a broad range of the spectrum,

from the near-infrared to well into the visible. They can be used as very efficient light emitting diodes and low threshold microlasers.[2]

In any macroscopic laser, spontaneous emission is a major source of energy loss, speed limitation and noise. The fraction of the spontaneous emission that is coupled into a single lasing mode can be increased by the enhancement and of spontaneous emission by the microcavity. The efficiency, emission rates, and photon statistics of light emitting diodes can all be controlled by forming microcavity resonators with sufficiently high Q values. Control of these properties will be welcome in a number of optoelectronic applications including flat panel electroluminescent displays and optical interconnects.

In the optoelectronics and microelectronics industry, silicon is the most widely used semiconductor not only in its crystalline, but also in its amorphous form. Being a direct band-gap material[6] unlike crystalline silicon,[7] amorphous silicon is unmatched as a photoreceptor for laser printing, as the material for switching elements in large area liquid crystal displays, for large photovoltaic panels and any other application that calls for a high quality semiconductor that can be processed on large areas or on curved or flexible substrates.[3]

It is generally agreed that the terms amorphous solid, non-crystalline solid, disordered solid, glass, or liquid have no precise structural meaning beyond the description that the structure is "not crystalline on any significant scale". The principal structural order present is imposed by the approximately constant separation of nearest-neighbor atoms or molecules.

Until the early time of 1970's, amorphous silicon prepared by evaporation or sputtering was not considered as one of the valuable semiconductor materials, because of large density of electronic states in the band gap related to a large density of structural defects.[4] The discovery of an amorphous silicon material prepared by the glow-discharge deposition of SiH_4 which can be doped and whose conductivity can be changed by ten orders of magnitude marked a turning point and opened a new research area.

Most interest is focused on hydrogenated amorphous silicon and its alloys, because hydrogen, by removing dangling bonds, eliminates non-radiative

recombination centers that are responsible for reduced luminescence efficiency (and reduced photovoltaic efficiency) and allows doping.[5] Another advantage of hydrogenated amorphous silicon is that it can deposited by plasma enhanced chemical vapor deposition (PECVD) onto almost any substrate at temperatures below 500 K, which makes it compatible with microelectronic technology.

In this research, planar hydrogenated amorphous silicon microcavities were fabricated. Microcavities were realized by embedding the active hydrogenated amorphous silicon layer between distributed Bragg reflectors which are composed of alternating silicon oxide and silicon nitride layers. All of the layers were grown by PECVD on silicon substrates. By tuning the cavity mode to emission maximum of amorphous silicon, a narrow and enhanced emission line is obtained.

After the introduction of the basic concepts in Chapter 1, a general theoretical background for resonant cavities is given in Chapter 2. Definitions of the fundamental parameters of microcavities, modified radiation pattern and lifetime of atoms in planar microcavities and the theory of transfer matrix method for the analysis of multilayer thin films are explained. Chapter 3, includes the considerations taken into account while designing the structures, and the fabrication process. In Chapter 4, the techniques used for characterizing the structures as well as the results of the measurements and calculations are presented. Finally, Chapter 5 concludes the work.

Chapter 2

Microcavity Theory

It's by now well known that the presence of a small optical cavity (microcavity) can significantly change the radiative behavior of an atom (or any optical gain medium) placed inside it. In a microcavity, two different resonant processes affect any spontaneous emission (SE) light intensity measurement. First, the microcavity acts as an optical resonator for light rays with specific wavelengths, which after one round trip, return to their starting position, i.e., resonate in the microcavity. These wavelengths correspond to the modes of the microcavity. As a consequence, if one of these modes is probed out of the cavity, a resonant change of SE light intensity must be detected. This effect, corresponding to a light intensity spatial redistribution, is observed even in the absence of any sizable resonant change of the average atomic spontaneous decay rate.[20] Much attention has been paid to the observation of cavity induced changes of SE decay rate,[22,24] because the lifetime changes are the most essential effect in the original concept of the modification of SE proposed by Purcell.[21] However, the rate of change of SE lifetime in one dimensionally confined microcavity structures has been predicted theoretically to be relatively small.[25]

2.1 Resonant Cavities

An optical resonator, the optical counterpart of an electronic resonant circuit, confines and stores light at certain resonance frequencies. It may be viewed as an optical transmission system incorporating feedback; light circulates or is repeatedly reflected within the system, without escaping. The simplest resonator is the planar-mirror resonator, often called as **Fabry-Perot resonator**, which comprises two parallel planar mirrors between which light is repeatedly reflected with little loss. Planar and spherical-mirror resonators, ring resonator, and optical-fiber resonator are the most typical optical resonators.

2.1.1 Resonator Modes

A monochromatic wave of frequency ν has a wavefunction[14]

$$u(\mathbf{r}, t) = Re\{U(\mathbf{r}) \exp(i2\pi\nu t)\}, \tag{2.1}$$

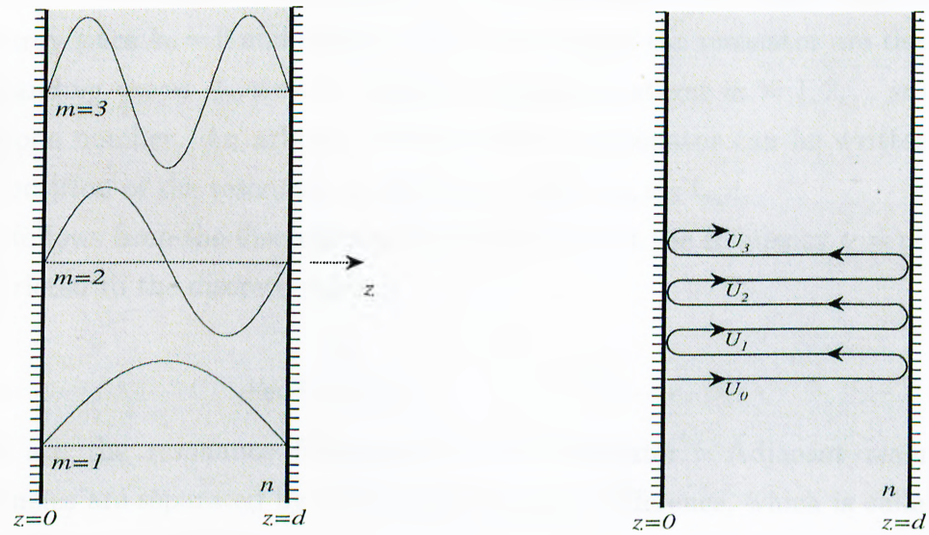

Figure 2.1: The Fabry-Perot resonator

which represents the transverse component of the electric field. The complex

amplitude $U(\mathbf{r})$ satisfies the Helmholtz equation, $\nabla^2 U + k^2 U = 0$, where $k = 2\pi\nu n/c$ is the wavenumber and n is the refractive index of the medium. The modes of the resonator are the basic solutions of the Helmholtz equation subject to the appropriate boundary conditions. For the planar-mirror resonator, the transverse components of the electric field vanish at the surfaces of the mirrors, so that $U(\mathbf{r}) = 0$ at the planes $z = 0$ and $z = d$ in Fig. 2.1. The standing wave

$$U(\mathbf{r}) = A \sin kz, \tag{2.2}$$

where A is a constant, satisfies the Helmholtz equation and vanishes at $z = 0$ and $z = d$ if k satisfies the condition $kd = m\pi$, where m is an integer. This restricts k to the values

$$k_m = \frac{m\pi}{d}, \tag{2.3}$$

so that the modes have complex amplitudes $U(\mathbf{r}) = A_m \sin k_m z$, where the A_m are constants. Negative values of m do not constitute independent modes since $\sin k_{-m} z = -\sin k_m z$. The value $m = 0$ is associated with a mode that carries no energy since $k_0 = 0$ and $\sin k_0 z = 0$. The modes of the resonator are therefore the standing waves $A_m \sin k_m z$, where the positive integer $m = 1, 2, \ldots$ is called the mode number. An arbitrary wave inside the resonator can be written as a superposition of the resonator modes, $U(\mathbf{r}) = \sum_m A_m \sin k_m z$.

It follows from the discreteness of k (Eq. 2.3) that the frequency $\nu = ck/2n\pi$ is restricted to the discrete values

$$\nu_m = m\frac{c}{2dn}, \qquad m = 1, 2, \ldots, \tag{2.4}$$

which are the resonance frequencies of the resonator. Adjacent resonance frequencies are separated by a constant frequency difference, which is called the free spectral range (FSR),

$$\nu_F = \nu_{m+1} - \nu_m = \frac{c}{2dn}. \tag{2.5}$$

The resonance wavelengths are of course, $\lambda_m = c/\nu_m = 2nd/m$. At resonance, the length of the resonator, $d = m\lambda/2n$, is an integer multiple of half wavelengths.

The resonator modes can alternatively be determined by following a wave as it travels back and forth between the two mirrors (See Fig. 2.1). A mode is a self-reproducing wave, i.e., a wave that reproduces itself after a single round-trip. The phase shift imparted by the two mirror reflections is 0 or 2π (π at each mirror). The phase shift imparted by a single round trip of propagation (a distance $2d$), $\varphi = k2d = 4\pi\nu dn/c$, must be a multiple of 2π,

$$\varphi = k2d = m2\pi, \qquad m = 1, 2, \ldots . \tag{2.6}$$

This leads to the relation $kd = m\pi$ and the resonance frequencies in 2.4. Therefore, only self-reproducing waves, or combinations of them, can exist within the resonator in the steady state. The total wave U is represented by the sum of an infinite number of phasors of equal magnitude,

$$U = U_0 + U_1 + U_2 + \ldots . \tag{2.7}$$

The phase difference of two consecutive phasors imparted by a single round-trip of propagation is $\varphi = k2d$. If the magnitude of the initial phasor is infinitesimal, the magnitude of each of these phasors must be infinitesimal. The magnitude of the sum of this infinite number of infinitesimal phasors is itself infinitesimal unless they are aligned, i.e., unless $\varphi = m2\pi$. Thus, an infinitesimal initial wave can result in the buildup of finite power in the resonator, but only if $\varphi = m2\pi$.

The strict condition on the frequencies of optical waves that are permitted to exist inside a resonator is relaxed when the resonator has losses. The phasors in Eq. 2.7 are not of equal magnitude in the presence of loss. The magnitude ratio of two consecutive phasors is the round-trip amplitude attenuation factor r introduced by the two mirror reflections and by the absorption in the medium. The intensity attenuation factor is therefore r^2. Thus $U_1 = hU_0$, where $h = re^{-i\varphi}$. The phasor U_2 is related to U_1 by this same complex factor h, as are all

consecutive factors. The net result is the superposition of an infinite number of waves, separated by equal phase shifts, but with amplitudes that are geometrically reduced. It is readily seen that $U = U_0 + U_1 + U_2 + ... = U_0 + hU_0 + h^2U_0 + ... = U_0(1 + h + h^2 + ...) = U_0/(1 - h)$. The transmitted intensity $I = |U|^2 = |U_0|^2 / |1 - re^{-i\varphi}|^2$ is found to be

$$I = \frac{I_{max}}{1 + (2\mathcal{F}/\pi)^2 \sin^2(\varphi/2)}. \tag{2.8}$$

Here $I_{max} = I_0/(1 - r)^2$, where $I_0 = |U_0|^2$ is the intensity of the initial wave, and

$$\mathcal{F} = \frac{\pi r^{1/2}}{1 - r} \tag{2.9}$$

is a parameter known as the **finesse** of the resonator.

The intensity is a periodic function of φ with period 2π. If F is large then I has sharp peaks centered about the values $\varphi = m2\pi$ (when all the phasors are aligned). The peaks have a full width at half maximum (FWHM) given by $\Delta\varphi = 2\pi/\mathcal{F}$.

The dependence of I on ν, which is the spectral response of the resonator, has a similar periodic behavior since $\varphi = k2d = 4\pi\nu dn/c$ is proportional to ν. This resonance profile,

$$I = \frac{I_{max}}{1 + (2\mathcal{F}/\pi)^2 \sin^2(\pi\nu/\nu_F)}, \tag{2.10}$$

is plotted in Fig. 2.2 for $\mathcal{F} = \infty$ and $\mathcal{F} = 10$, where $\nu_F = c/2dn$. The maximum $I = I_{max}$ is achieved at the resonance frequencies

$$\nu = \nu_m = m\nu_F, \qquad m = 1, 2, ... , \tag{2.11}$$

whereas the minimum value

$$I = \frac{I_{max}}{1 + (2\mathcal{F}/\pi)^2}, \tag{2.12}$$

occurs at the midpoints between the resonances. When the finesse is large ($\mathcal{F} \gg 1$), the resonator spectral response is sharply peaked about the resonance

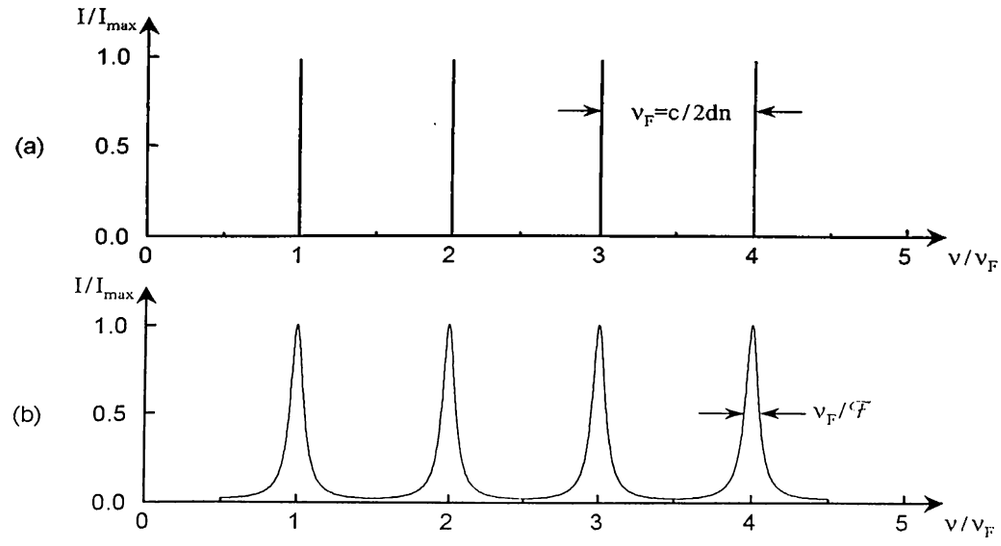

Figure 2.2: (*a*) A lossless resonator ($\mathcal{F} = \infty$) in the steady state can sustain light waves only at the precise resonance frequencies ν_m. (*b*) A lossy resonator ($\mathcal{F} = 10$) sustains waves at all frequencies, but the attenuation resulting from the destructive interference increases at frequencies away from the resonances.

frequencies and I_{min}/I_{max} is small. The FWHM of the resonance peak is $\delta\nu = (c/4\pi dn)\Delta\varphi = \nu_F/\mathcal{F}$.

2.1.2 Sources of Resonator Loss

The two principal source of loss in optical resonators are the absorption and scattering in the medium between the mirrors and the imperfect reflection at the mirrors. There are two underlying sources of reduced reflection; a partially transmitting mirror is often used in a resonator to permit the light to escape from it, and the finite size of the mirrors causes a fraction of the light to leak around the mirrors.

For mirrors of reflectances $R_1 = r_1^2$ and $R_2 = r_2^2$, the wave intensity decreases by the factor R_1R_2 in the course of the two reflections associated with a single round trip. The overall intensity attenuation factor is therefore

$$r^2 = R_1 R_2 \exp(-2\alpha_s d), \tag{2.13}$$

which is usually written in the form

$$r^2 = \exp(-2\alpha_r d), \tag{2.14}$$

where α_r is the overall distributed-loss coefficient. Equations 2.13 and 2.14 provide

$$\alpha_r = \alpha_s + \alpha_1 + \alpha_2 = \alpha_s + \frac{1}{2d} \ln \frac{1}{R_1 R_2}. \tag{2.15}$$

where $\alpha_1 = \frac{1}{2d} \ln \frac{1}{R_1}$ and $\alpha_2 = \frac{1}{2d} \ln \frac{1}{R_2}$ represent the loss coefficients attributed to mirrors 1 and 2, respectively.

The finesse $\mathcal{F}$ can be expressed as a function of the effective loss coefficient α_r by substituting 2.14 in 2.9, which yields

$$\mathcal{F} = \frac{\pi \exp(\alpha_r d/2)}{1 - \exp(-\alpha_r d)}. \tag{2.16}$$

If the loss factor is small, $\alpha_r d \ll 1$, then $\exp(-\alpha_r d) \simeq 1 - \alpha_r d$, whereupon

$$\mathcal{F} = \frac{\pi}{\alpha_r d}. \tag{2.17}$$

This shows that the finesse decreases with increasing loss.

2.1.3 Cavity Q Values

The quality factor is often used to characterize electrical resonance circuits and resonators. This parameter is defined as[14,19]

$$Q = \frac{2\pi(stored\ energy)}{energy\ loss\ per\ cycle}. \tag{2.18}$$

Large Q factors are associated with low loss resonators.

The Q factor of an optical resonator may be determined by observing that stored energy is lost at the rate $(c/n)\alpha_r$(per unit time), which is $(c/n)\alpha_r/\nu_0$ (per cycle), so that

$$Q = \frac{2\pi}{[(c/n)\alpha_r/\nu_0]}, \tag{2.19}$$

Since $\delta\nu = \nu_F/\mathcal{F} = c\alpha_r/2n\pi$,

$$Q = \frac{\nu_0}{\delta\nu}. \tag{2.20}$$

Using $\nu = c/\lambda$, and $\delta\nu = -c\delta\lambda/\lambda^2$, this can be written in terms of λ and $\delta\lambda$

$$Q = \frac{\lambda_0}{\delta\lambda}. \tag{2.21}$$

2.1.4 Density of Modes

The effects associated with radiation in cavities are best quantified using Fermi's golden rule. Ignoring the possibility of photon reabsorption, the radiative transition rate $W_{e\to g}$ of an atom from an excited to the ground state can be written

$$W_{e\to g} = \frac{2\pi}{\hbar^2}|M|^2 g(k), \tag{2.22}$$

where M is the atom-vacuum field matrix element, and $g(k)$ is the effective mode density for the optical field.

In free space, $g(k)$ increases quadratically with wavenumber

$$g_f(k)dk = \frac{1}{3\pi^2}k^2 dk \tag{2.23}$$

For a planar mirror microcavity we must consider two possible orientations of the dipole: parallel, and perpendicular to the z axis (suppose that the mirrors are defined by the planes $z = \pm L/2$). Mode densities are given by[13]

$$g_{\|}(k)dk = \frac{1}{2\pi^2}k_c k\left[1 + 2\left[p - \frac{1}{6}\left(\frac{2k_c}{k}\right)^2 p(p+1)(2p+1)\right]\right], \tag{2.24}$$

and

$$g_{\perp}(k)dk = \frac{1}{2\pi^2}k_c k\left[q + \left(\frac{k_c}{k}\right)^2\left(\frac{4}{3}q^3 - \frac{1}{3}q\right)\right], \tag{2.25}$$

where $k_c = \pi/L$, p and q denote the largest integer less than or equal to $k/2k_c$ and $(k/k_c + 1)/2$, respectively. Those functions are plotted in Fig. 2.3.

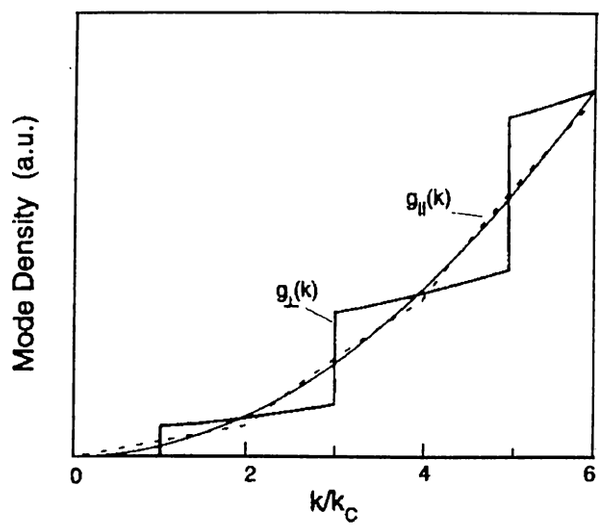

Figure 2.3: Modes in a loss free planar microcavity. The parallel dipole mode density is represented by the dashed line, whereas the perpendicular dipole is the staircase curve. Also shown is the free space mode density which varies quadratically with frequency.

2.2 Spontaneous Emission Patterns of an Atom in Free Space

Let us consider a dipole moment along the x axis in a polar coordinate (r,ψ,γ) shown in Figure 2.4. The dipole emits electromagnetic fields having both perpendicular (s wave) and parallel (p wave) to the emission plane. The radiation intensity at the point (r,ψ,γ) is[10,9]

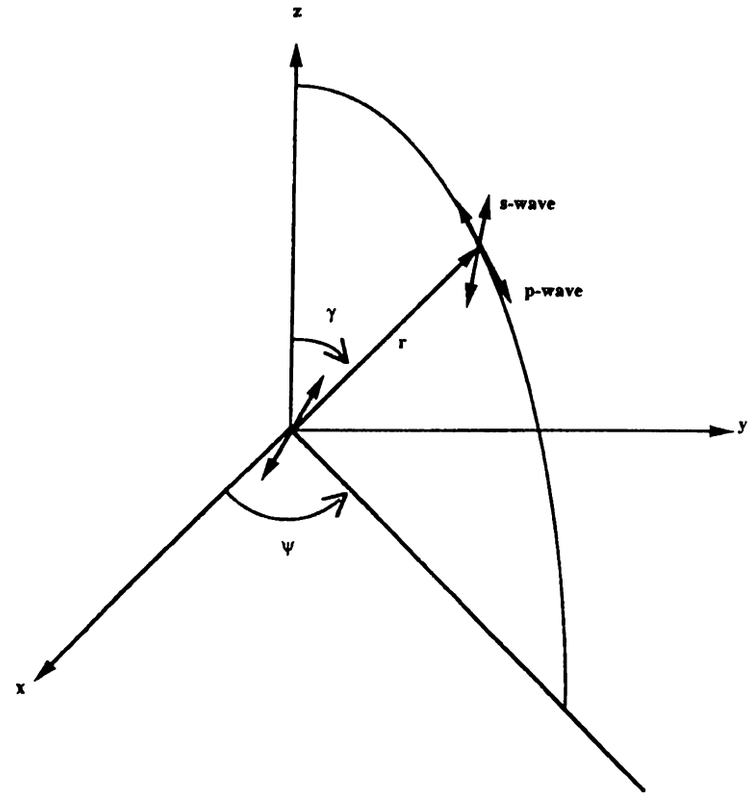

Figure 2.4: Polar coordinates (r,ψ,γ) for radiation pattern calculation.

$$dI(r,\psi,\gamma) = \eta\frac{P_{12}^2 E_0^2}{r^2} \times \begin{cases} \sin^2\psi & s \text{ wave} \\ \cos^2\psi\cos^2\gamma & p \text{ wave} \end{cases} \tag{2.26}$$

Here η is a constant and E_0^2 is the vacuum field intensity at the location ($r = 0$) of a dipole moment. In free space, E_0^2 is independent of ψ and γ (isotropic). The total emitted intensity is given by

$$I \equiv \int_0^{2\pi} d\psi \int_0^{\pi} d\gamma\, r^2\, \sin\gamma\, dI(r,\psi,\gamma) = \frac{8}{3}\pi\eta P_{12}^2 E_0^2 \tag{2.27}$$

Three-fourths of Eq. 2.27 is radiated as the s wave and the one-fourth as the p wave. When the dipole moment is along the y axis, the result is exactly the same.

If the dipole moment is along the z axis, the radiation intensity at the point (r,ψ,γ) is[9]

$$dI(r,\psi,\gamma) = \eta\frac{P_{12}^2 E_0^2}{r^2} \times \begin{cases} 0 & s \text{ wave} \\ \sin^2\psi & p \text{ wave} \end{cases} \tag{2.28}$$

The total emitted intensity,

$$I \equiv \int_0^{2\pi} d\psi \int_0^{\pi} d\gamma\ r^2\ \sin\gamma\ dI(r,\psi,\gamma) = \frac{8}{3}\pi\eta P_{12}^2 E_0^2 \tag{2.29}$$

is equal to Eq. 2.27 for the dipole moment along the x axis, as it should be, but in this case, all the emitted power is carried by the p wave. The choice of the emission plane including the z axis employed here, thus the definition of the s wave and the p wave, has no physical significance in free space. However, as discussed in subsequent sections, the vacuum field intensity E_0^2 in one-dimensional periodic structures becomes a function of not only the angle γ but also the polarization direction (s or p).

2.3 Spontaneous Emission of an Atom Between Ideal Mirrors

We consider the spontaneous emission of an atom placed between two hypothetical ideal mirrors in this section. Assume that a mirror has constant reflection and transmission coefficients and phase shift, which are all independent of incident angle γ. Even though such a mirror is not realistic, it still gives a simple physical picture for the enhanced and inhibited spontaneous emission realized by one-dimensional periodic structures.

Let us consider the modification of the vacuum field intensity E_0^2 by the presence of two planar mirrors shown in Figure 2.5. The two field amplitudes A_+ and A_- at the location of the atom ($z = 0$) are

$$A_+ = \frac{\sqrt{T}\exp(ikz_0\cos\gamma)}{1 - R\exp[i(2kd\cos\gamma + 2\phi_r)]}E_0 \tag{2.30}$$

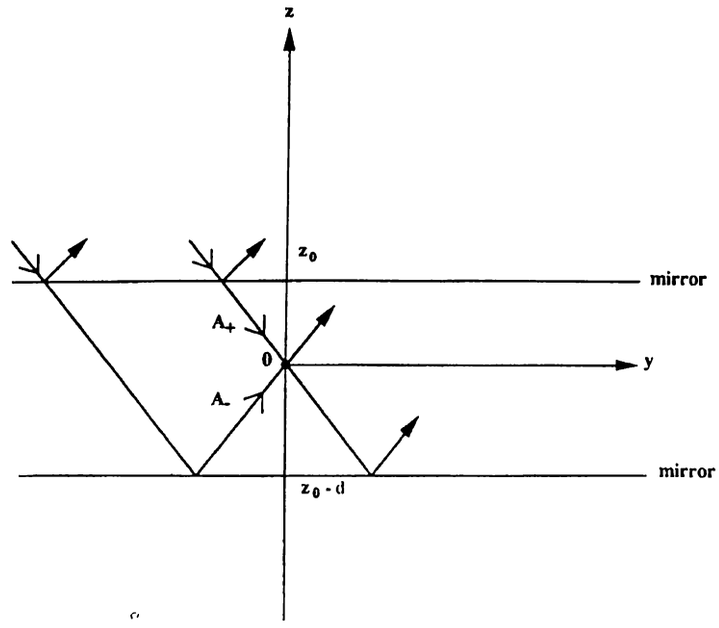

Figure 2.5: An atom between two planar mirrors.

and

$$A_- = \frac{\sqrt{RT}\exp[i\{k(2d - z_0)\cos\gamma + \phi_r\}]}{1 - R\exp[i(2kd\cos\gamma + 2\phi_r)]}E_0 \tag{2.31}$$

where R and T are the reflection and transmission coefficients, ϕ_r is the phase shift due to reflection, d is the mirror spacing, and z_0 is the distance between the upper mirror and the atom.

If the dipole moment is along the z axis, the vacuum field intensity coupled with the dipole is modified according to

$$E_z^2 = |A_+ - A_-|^2 = \{|A_+|^2 + |A_-|^2 - 2\,|A_+|\,|A_-|\cos\phi\}E_0^2 \tag{2.32}$$

where

$$\phi = 2k(d - z_0)\cos\gamma + \phi_r \tag{2.33}$$

If the dipole moment is along the x axis or y axis, the vacuum field intensity coupled with the dipole is modified according to

$$E_x^2 = E_y^2 = |A_+ + A_-|^2 = \{|A_+|^2 + |A_-|^2 + 2\,|A_+|\,|A_-|\cos\phi\}E_0^2 \tag{2.34}$$

2.3.1 Modified Radiation Pattern and Lifetime in a Half-Wavelength Cavity

If the phase shift ϕ_r due to reflection is π, the horizontal dipole (P_x or P_y) couples only with odd modes and the vertical dipole (P_z) couples only with even modes. Suppose the two mirrors are separated by a distance equal to half a wavelength, $d = \lambda/2$, and the atom is located midway between the two mirrors, $z_0 = \lambda/4$. The atom is located at the antinode of the horizontal field of a resonant standing wave ($N = 1$ odd mode) propagating along the z axis, so that the spontaneous emission in the z axis by the horizontal dipole should be enhanced. The horizontal component of the vacuum field intensity E_x^2 (E_y^2) propagating in the direction γ for the dipole moment along the x axis (y axis) is

$$E_x^2 = E_y^2 = \frac{T\{1 + R + 2\sqrt{R}\cos[\pi(\cos\gamma + 1)]\}}{(1-R)^2 + 4R\sin^2[\pi(\cos\gamma + 1)]}E_0^2 \tag{2.35}$$

The radiation intensity at the point (r,ψ,γ) is calculated by using Eq. 2.35 for E_0^2 in Eq. 2.26:

$$dI(r,\psi,\gamma) = \eta\frac{P_{12}^2E_0^2}{r^2}\cdot\frac{(1-R)\{1 + R + 2\sqrt{R}\cos[\pi(\cos\gamma + 1)]\}}{(1-R)^2 + 4R\sin^2[\pi(\cos\gamma + 1)]} \times \begin{cases} \sin^2\psi & s \text{ wave} \\ \cos^2\psi\cos^2\gamma & p \text{ wave} \end{cases} \tag{2.36}$$

Numerical examples of the radiation pattern in Eq. 2.36 for $T = 0.05$ and $R = 0.95$ are plotted in Figure 2.6. The radiation patterns in both polarizations concentrate on $\gamma \simeq 0$, as expected. In a small γ value where the radiation field intensity is appreciable, Eq. 2.36 is approximated by

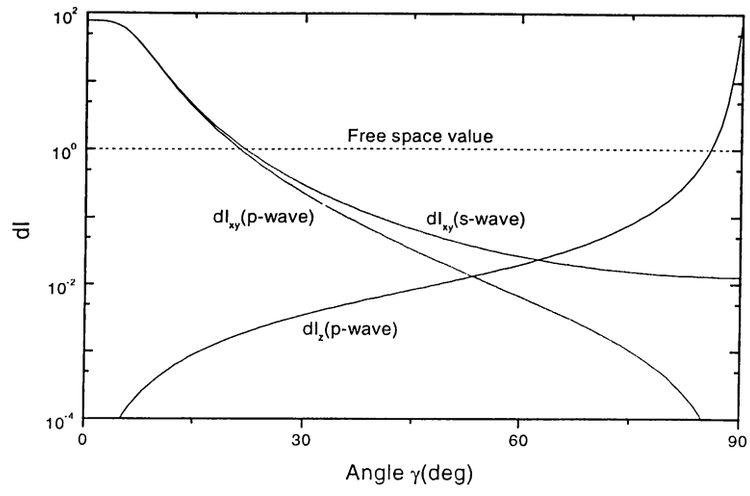

Figure 2.6: Spontaneous emission patterns from an atom between two ideal mirrors with $d = \lambda/2$, $R = 0.95$, and $\phi_r = \pi$.

$$dI(r,\psi,\gamma) = \eta\frac{P_{12}^2 E_0^2}{r^2}\cdot\frac{4(1-R)}{(1-R)^2+\pi^2 R\gamma^4}\times\begin{cases}\sin^2\psi & s \text{ wave}\\ \cos^2\psi & p \text{ wave}\end{cases} \tag{2.37}$$

The peak intensity at $\gamma = 0$ is enhanced by a factor of $4/(1-R)$ above the free space value and the diverging angle of the main lobe is $\sqrt{(1-R)/\pi}$. The total intensity of emission in all directions is given by

$$I = 2\int_0^{2\pi} d\psi \int_0^{\pi/2} d\gamma\, r^2\, \sin\gamma\, dI(r,\psi,\gamma) \simeq 4\pi\eta P_{12}^2 E_0^2 \tag{2.38}$$

Here the integral formula $\int_0^\infty x/(1+x^4)\, dx = \pi/4$ and $sin\gamma \simeq \gamma$ are used. The total emitted power is 1.5 times larger than the free-space value, which means that the spontaneous lifetime is reduced by a factor of $\frac{2}{3}$. This change in the spontaneous lifetime is independent of the reflection coefficient R. The spontaneous emission is carried equally by the p and the s wave.

The vertical component of the vacuum field intensity E_z^2 propagating in the direction γ for the dipole moment along the z axis is, on the other hand, given

by

$$E_x^2 = E_y^2 = \frac{T\{1+R-2\sqrt{R}\cos[\pi(\cos\gamma+1)]\}}{(1-R)^2+4R\sin^2[\pi(\cos\gamma+1)]}E_0^2 \tag{2.39}$$

The radiation intensity at the point (r,ψ,γ) is given by Eqs. 2.39 and 2.28:

$$dI(r,\psi,\gamma) = \eta\frac{P_{12}^2E_0^2}{r^2}\cdot\frac{(1-R)\{1+R-2\sqrt{R}\cos[\pi(\cos\gamma+1)]\}}{(1-R)^2+4R\sin^2[\pi(\cos\gamma+1)]} \times\begin{cases}0 & s \text{ wave}\\ \sin^2\gamma & p \text{ wave}\end{cases} \tag{2.40}$$

The numerical example of the radiation pattern in Eq. 2.40 is also plotted in Figure 2.6. The radiation pattern concentrates on $\gamma \simeq \pi/2$. This is because the vertical dipole couples with an $N = 0$ even mode that propagates within the $x-y$ plane. In a γ value close to $\pi/2$ where the radiation intensity is appreciable, Eq. 2.40 is approximated by

$$dI(r,\psi,\gamma) = \eta\frac{P_{12}^2E_0^2}{r^2}\cdot\frac{4(1-R)}{(1-R)^2+4\pi^2R(\pi/2-\gamma)^2}\times\begin{cases}0 & s \text{ wave}\\ \sin^2\gamma & p \text{ wave}\end{cases} \tag{2.41}$$

The peak intensity at $\gamma = \pi/2$ is enhanced by a factor $4/(1-R)$ above the free space value and the diverging angle centered at $\gamma = \pi/2$ is $(1-R)/2\pi$. The total intensity of emission in all directions is given by

$$I = 2\int_0^{2\pi}d\psi\int_0^{\pi/2}d\gamma\; r^2\;\sin\gamma\; dI(r,\psi,\gamma) \simeq 4\pi\eta P_{12}^2E_0^2 \tag{2.42}$$

Here the integral formula $\int_0^\infty dx/(ax^2+b) = \pi/2\sqrt{ab}$ is used. The total emitted power is again 1.5 times larger (the spontaneous lifetime is shorter by a factor $\frac{2}{3}$) than the free-space value. The spontaneous emission is carried only by the p wave.

2.3.2 Modified Radiation Pattern and Lifetime in a One-Wavelength Cavity

Next let us consider the case where the two mirrors are separated by a distance equal to one wavelength, $d = \lambda$, and the atom is again located between the two mirrors, $z_0 = \lambda/2$. If the phase shift ϕ_r due to reflection is zero, the horizontal dipole couples with even modes and the vertical dipole couples with odd modes.[11] The atom is located at the antinode of the horizontal field component of a resonant standing wave ($N = 2$ even mode) propagating along the z axis. Therefore, the spontaneous emission in the z direction by the horizontal dipole is expected to be enhanced in this case also. The vacuum field intensity E_x^2 (E_y^2) for the dipole moment along the x axis (y axis) is

$$E_x^2 = E_y^2 = \frac{T\{1 + R + 2\sqrt{R}\cos(2\pi\cos\gamma)\}}{(1-R)^2 + 4R\sin^2(2\pi\cos\gamma)} E_0^2 \tag{2.43}$$

The radiation intensity at the point (r,ψ,γ) is

$$dI(r,\psi,\gamma) = \eta\frac{P_{12}^2 E_0^2}{r^2} \cdot \frac{(1-R)\{1 + R + 2\sqrt{R}\cos(2\pi\cos\gamma)\}}{(1-R)^2 + 4R\sin^2(2\pi\cos\gamma)} \times \begin{cases} \sin^2\psi & s \text{ wave} \\ \cos^2\psi\cos^2\gamma & p \text{ wave} \end{cases} \tag{2.44}$$

The radiation pattern concentrates on $\gamma \simeq 0$ and also on $\gamma \simeq \pi/2$, as shown in Fig. 2.7. The radiation peak near $\gamma = \pi/2$ is due to the $N = 0$ even mode propagating within the x-y plane. In a small γ value where the radiation field intensity is appreciable, Eq. 2.44 is approximated by

$$dI(r,\psi,\gamma) = \eta\frac{P_{12}^2 E_0^2}{r^2} \cdot \frac{4(1-R)}{(1-R)^2 + 4\pi^2 R\gamma^4} \times \begin{cases} \sin^2\psi & s \text{ wave} \\ \cos^2\psi & p \text{ wave} \end{cases} \tag{2.45}$$

Comparing Eq. 2.45 with Eq. 2.37, the peak intensity is enhanced by the same factor $4/(1-R)$ above the free space value, but the diverging angle of the main lobe is reduced by a factor of $\sqrt{2}$, that is, to $\sqrt{(1-R)/2\pi}$ for the one-wavelength

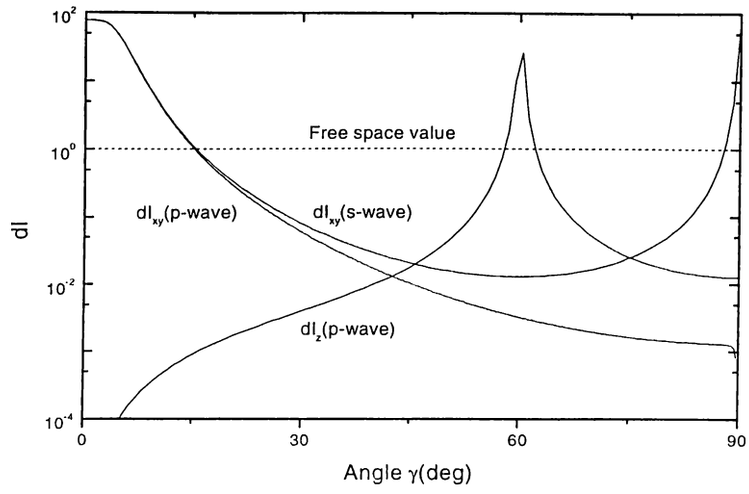

Figure 2.7: Spontaneous emission patterns from an atom between two ideal mirrors with $d = \lambda$, $R = 0.95$, and $\phi_r = 0$.

cavity from $\sqrt{(1-R)/\pi}$ for the half-wavelength cavity. The integrated emission intensity is given by

$$I \simeq 2\pi\eta P_{12}^2 E_0^2 \tag{2.46}$$

In a γ value region close to $\pi/2$ where the radiation intensity is also appreciable, Eq. 2.44 is approximated by

$$dI(r,\psi,\gamma) = \eta\frac{P_{12}^2 E_0^2}{r^2}\cdot\frac{4(1-R)}{(1-R)^2+16\pi^2 R(\pi/2-\gamma)^2}\times\begin{cases}\sin^2\psi & s \text{ wave}\\ 0 & p \text{ wave}\end{cases} \tag{2.47}$$

The peak intensity in s polarization at $\gamma = \pi/2$ is enhanced by a factor of $4/(1-R)$ above the free space value and the diverging angle is $\sqrt{(1-R)/4\pi}$. The integrated emission intensity is

$$I \simeq \pi\eta P_{12}^2 E_0^2 \tag{2.48}$$

The total emitted power is $I \simeq 3\pi\eta P_{12}^2 E_0^2$, which is larger than the free-space value by a factor of $\frac{9}{8}$; the spontaneous lifetime is decreased by a factor of $\frac{8}{9}$. This factor is again independent of the reflection coefficient R.

The vacuum field intensity E_z^2 for the dipole moment along the z axis is

$$E_x^2 = E_y^2 = \frac{T\{1 + R - 2\sqrt{R}\cos(2\pi\cos\gamma)\}}{(1-R)^2 + 4R\sin^2(2\pi\cos\gamma)} E_0^2 \tag{2.49}$$

The radiation intensity at the point (r,ψ,γ) is

$$dI(r,\psi,\gamma) = \eta\frac{P_{12}^2 E_0^2}{r^2} \cdot \frac{(1-R)\{1 + R - 2\sqrt{R}\cos(2\pi\cos\gamma)\}}{(1-R)^2 + 4R\sin^2(2\pi\cos\gamma)} \times \begin{cases} 0 & s \text{ wave} \\ \sin^2\gamma & p \text{ wave} \end{cases} \tag{2.50}$$

The intensity of total emission is given by

$$I \simeq 3\pi\eta P_{12}^2 E_0^2 \tag{2.51}$$

The total emitted power is larger than the free-space value by a factor of $\frac{9}{8}$; the spontaneous lifetime is decreased by a factor of $\frac{8}{9}$.

As shown above, the spontaneous emission from the horizontal dipole moment along the x axis or y axis can be concentrated on $\gamma \simeq 0$ by the half-wavelength cavity with $\phi_r = \pi$. This is a very useful feature for an efficient surface emitting laser. The spontaneous emission from the vertical dipole moment along the z axis can be concentrated on $\gamma \simeq \pi/2$ by the half-wavelength cavity with $\phi_r = \pi$. This is a very useful feature for an efficient edge emitting laser. The one-wavelength cavity with $\phi_r = 0$, however, has either two emission peaks (horizontal dipole) or one peak emission in the oblique (60°) direction, and so it is less interesting for those device applications.

2.4 Analysis of Multilayer Thin Films

If electromagnetic radiation falls onto a structure consisting of thin films of several different materials, multiple reflections will take place within the structure. Exact analysis for the electromagnetic wave propagation in such structures can be done by the computer-aided transfer matrix method (TMM).[15-17]

Consider a plane wave, with a *vacuo* wavelength λ_0,and of infinite extent, incident on a multilayer film. At the first surface, some of the energy will be reflected and some will be transmitted, as shown in Figure 2.8, where $\mathbf{k}$, $\mathbf{k}'$ and $\mathbf{k}''$ represent the vectors of the incident, refracted and reflected waves, respectively; the subscript indicates the surface number.

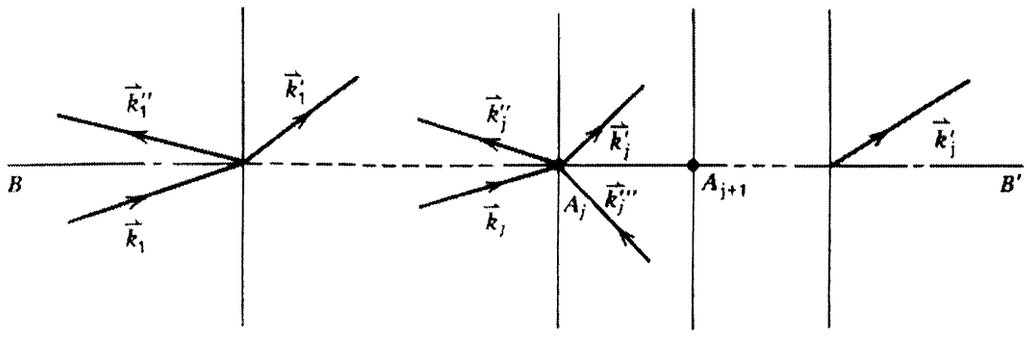

Figure 2.8: Ray paths in a multilayer film.

Boundary conditions at the jth interface yields for the field components perpendicular to the plane of incidence;

$$E_{\perp j} + E''_{\perp j} = E'_{\perp j} + E'''_{\perp j} = E_{\perp j+1} e^{-i\phi_j} + E''_{\perp j+1} e^{i\phi_j}. \tag{2.52}$$

Here $E'''_{\perp j}$ is the electric field at A_j due to the wave reflected at the $(j+1)$th interface. Last equality follows from the identity of the wave pairs $(\mathbf{k}'_j, \mathbf{k}_{j+1})$ and $(\mathbf{k}'''_j, \mathbf{k}''_{j+1})$. $\mathbf{k}'''_j$ refers to the wave incident on surface j after reflection from surface $j+1$. The phase shift ϕ_j relates the wave at A_j to the corresponding one at A_{j+1} and is given by

$$\phi_j = k_j d_j cos\theta_j = \frac{2\pi n_j d_j \cos\theta_j}{\lambda_0}, \tag{2.53}$$

where $k_j = |\mathbf{k}_j|$

d_j is the thickness of the layer following the jth surface,

n_j is its refractive index, and

θ_j is the angle between k_j' and the film normal, BB'.

The corresponding equation for the magnetic field vectors are

$$\begin{aligned} n_{j-1}\cos\theta_{j-1}(E_{\perp j} - E_{\perp j}'') &= n_j \cos\theta_j (E_{\perp j}' - E_{\perp j}''') \\ &= n_j \cos\theta_j (E_{\perp j+1} e^{-i\phi_j} - E_{\perp j+1}'' e^{i\phi_j}). \end{aligned} \tag{2.54}$$

For the electric field components parallel to the plane of incidence, the corresponding equations are

$$\cos\theta_{j-1}(E_{\|j} + E_{\|j}'') = \cos\theta_j (E_{\|j+1} e^{-i\phi_j} + E_{\|j+1}'' e^{i\phi_j}) \tag{2.55}$$

and

$$n_{j-1}(E_{\|j} - E_{\|j}'') = n_j (E_{\|j+1} e^{-i\phi_j} - E_{\|j+1}'' e^{i\phi_j}). \tag{2.56}$$

Those four equations can be simplified by writing the tangential field component

$$E_{t_j} = E_{\perp j} \tag{2.57}$$

for the component perpendicular to the plane of incidence, and

$$E_{t_j} = E_{\|j} \cos\theta_{j-1} \tag{2.58}$$

for the one parallel. In terms of E_t then

$$E_{t_j} + E_{t_j}'' = E_{t_{j+1}} e^{-i\phi_j} + E_{t_{j+1}}'' e^{i\phi_j} \tag{2.59}$$

and

$$E_{t_j} - E''_{t_j} = c_j(E_{t_{j+1}}e^{-i\phi_j} - E''_{t_{j+1}}e^{i\phi_j}), \tag{2.60}$$

where

$$c_j = \frac{n_j \cos\theta_j}{n_{j-1}\cos\theta_{j-1}}, \qquad \frac{n_j \cos\theta_{j-1}}{n_{j-1}\cos\theta_j}, \tag{2.61}$$

respectively for the perpendicular and parallel components.

Solving 2.59 and 2.60, we find the incident and the reflected waves

$$E_{t_j} = \frac{1}{2}[(1+c_j)E_{t_{j+1}}e^{-i\phi_j} + (1-c_j)E''_{t_{j+1}}e^{i\phi_j}] \tag{2.62}$$

$$E''_{t_j} = \frac{1}{2}[(1-c_j)E_{t_{j+1}}e^{-i\phi_j} + (1+c_j)E''_{t_{j+1}}e^{i\phi_j}]. \tag{2.63}$$

To solve these equations for a given multilayer film consisting of a total of N layers (including substrate and surface medium), we compute the fields backwards, starting with

$$E_{t_N} = A, \qquad E''_N = 0, \tag{2.64}$$

since there is no reflection from the right-hand boundary of the last medium. On substituting these into 2.62 and 2.63, we obtain $E_{t_{N-1}}, E''_{t_{N-1}}$. From these, the preceding E_t's may be calculated, until E_{t_1}, E''_{t_1} are found in terms of A.

Matrix notation provides a convenient shorthand formulation here, Eqs. 2.62 and 2.63 becomes

$$\begin{pmatrix} E_{t_j} \\ E''_{t_j} \end{pmatrix} = \mathbf{M}_j \begin{pmatrix} E_{t_{j+1}} \\ E''_{t_{j+1}} \end{pmatrix} \tag{2.65}$$

where

$$\mathbf{M}_j = \begin{pmatrix} (1+c_j)e^{-i\phi_j} & (1-c_j)e^{i\phi_j} \\ (1-c_j)e^{-i\phi_j} & (1+c_j)e^{i\phi_j} \end{pmatrix}. \tag{2.66}$$

In this notation, E_{t_1} and E''_{t_1} are given in terms of $E_{t_N} = A$ as

$$\begin{pmatrix} E_{t_1} \\ E''_{t_1} \end{pmatrix} = \prod_{1}^{N-1} \mathbf{M}_j \begin{pmatrix} E_{t_N} \\ 0 \end{pmatrix} \tag{2.67}$$

The film reflectance and transmittance, respectively, are then given by

$$R = \left| \frac{E''_{t_1}}{E_{t_1}} \right|^2 \tag{2.68}$$

and

$$T = \left| \frac{A}{E_{t_1}} \right|^2 \frac{n'}{n}, \tag{2.69}$$

where n, n' are the refractive indices in the media preceding and following the multilayer film, respectively.

In an absorbing medium, with absorption coefficient α and refractive index n_R, the field amplitude may be written

$$\frac{E(z)}{E(0)} = e^{-(1/2)\alpha z} e^{in_R k_0 z} = e^{i\hat{n}k_0 z} \tag{2.70}$$

where

$$\hat{n} = n_R + \frac{i\alpha}{2k_0} \tag{2.71}$$

is called the *complex refractive index.* The use of $\hat{n}$ permits the results for nonabsorbing layers to be applied to absorbing layers as well.

2.4.1 Quarter-Wave Stack Analysis

The simplest nontrivial periodic multilayer system to analyze is the one whose period consists of two layers of differing refractive indices n_1, n_2 both having the same optical thickness

$$d_0 = d_j n_j, \qquad j = 1, 2 \tag{2.72}$$

where d_j is the geometrical thickness of the layer having refractive index n_j. Such a system has a reflectance maximum at the wavelength, say λ_0, for which d_0 is one-quarter of λ_0 and is called *simple quarter-wave stack* or *distributed Bragg reflector* (DBR). The response of a number of SiO_2 and Si_3N_4 quarter-wave stacks, which are used in our devices as mirrors of the Fabry-Perot cavity, calculated by TMM is shown in Fig. 2.9 as a function of the (normalized) reciprocal wavelength. This figure illustrates that, as the number (N) of periods in the stack increases, the reflectance at λ_0 approaches unity, the transition from reflection to transmission becomes sharper, and the number of oscillations outside the rejection band increases. As N approaches infinity, the reflectance approaches unity over a band, the high-reflectance zone, given by[18]

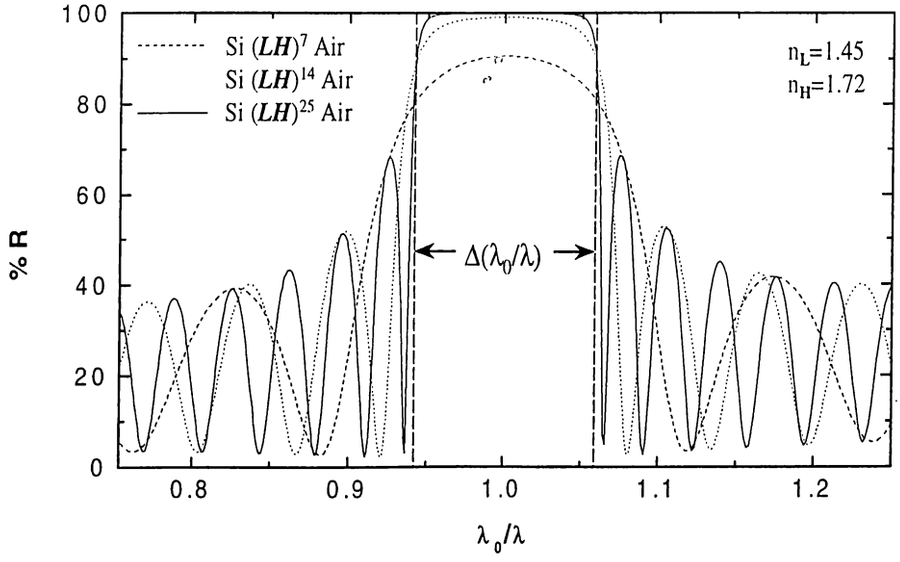

Figure 2.9: Calculated reflectance curves of quarter-wave stacks of type $(LH)^N$. L and H stand for low (SiO_2) and high (Si_3N_4) refractive index layers of quarter wave thickness at $\lambda_0 = 715$ nm. Index ratio is $n_L/n_H = 0.84$.

$$\Delta\left(\frac{\lambda_0}{\lambda}\right) = \frac{4}{\pi}\sin^{-1}\left|\frac{(1-n_L/n_H)}{(1+n_L/n_H)}\right| \tag{2.73}$$

which is equal to 0.11 for SiO_2 and Si_3N_4 pairs (See Fig. 2.9).

The reflectance maximum of the quarter wave stack is given by[15]

$$R_{max} = \frac{P + P^{-1} - 2}{P + P^{-1} + 2}, \tag{2.74}$$

where $P = (n_L/n_H)^{2N}(n_0/n_s)$, and n_s and n_0 are the refractive indices of the substrate and the medium above the stack respectively. For $N = 7$, $N = 10$ and $N = 14$, this gives a reflectance maximum of 90.7%, 96.5% and 99.1%, respectively (See Fig. 2.9). Clearly, the ratio n_L/n_H controls both the width of the high-reflectance band and the rate at which the reflectance approaches unity.

2.4.2 Microcavity Analysis

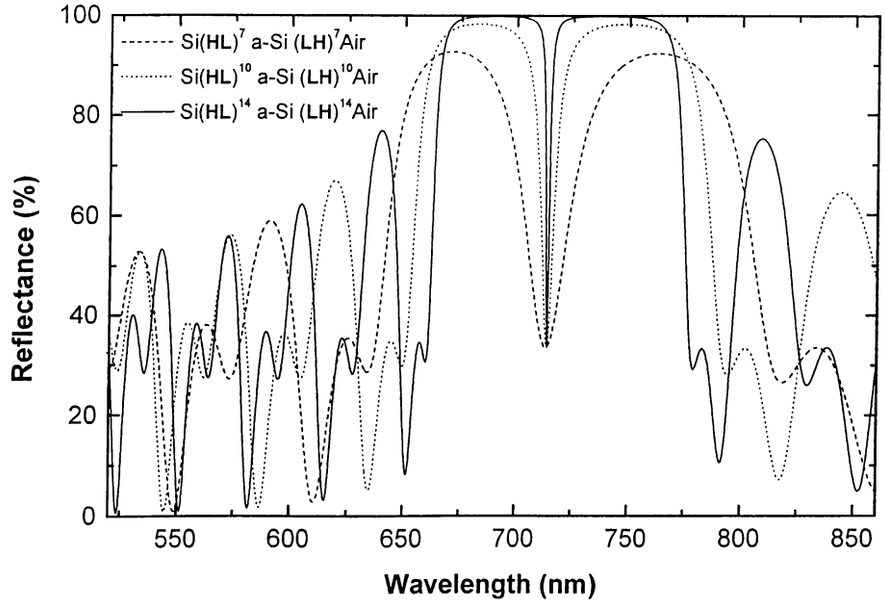

Figure 2.10: Calculated reflectance curves of microcavities with 7, 10, and 14 pairs of DBR layers on both sides. L and H stand for low (SiO_2) and high (Si_3N_4) refractive index layers of quarter wave thickness at $\lambda_0 = 715$ nm. The optical thickness of the active amorphous silicon layer (n=2.18) is $\lambda_0/2$.

The response of a number of microcavities with different Ns (number of

periods in the quarter wave stack), calculated by TMM is shown in Fig. 2.10. This figure illustrates that as reflectance of the mirrors increases (reflectance approaches unity as the number of periods in the stack increases, see Fig. 2.9), the resonant transmission bandwidth decreases. This results in high quality factors.

The quality factor is a function of the effective loss coefficient α_r, and the relation is given by Eq. 2.19. α_r is given by Eq. 2.15. Assuming $\alpha_s \simeq 0$ at resonance wavelength, $\alpha_r = \frac{1}{2d} \ln \frac{1}{R_1 R_2}$. Substituting in Eq. 2.19

$$Q = \frac{2\pi}{(\lambda_0/2nd) \ln(1/R_1 R_2)}. \tag{2.75}$$

d is the geometrical thickness of the cavity. For a half wavelength cavity $d = \lambda_0/2n$, then $Q = 2\pi/\ln(1/R_1 R_2)$.

For the cavity with 10 pairs of DBR layers on both sides for example, $R_1 = R_2 = 0.965$ (See Fig. 2.9). This gives a quality factor of 88 and using $Q = \frac{\lambda_0}{\delta\lambda}$, a resonant transmission bandwidth of 8 nm. The cavities with 7 and 14 pairs of DBR layers have quality factors of 32 and 313, which give resonant transmission bandwidths of 22 nm and 2.3 nm, respectively.

Chapter 3

Design and Fabrication

3.1 Microcavity Design

The fabricated planar Fabry-Perot microcavity consists of a $\lambda/2$ or λ thick hydrogenated amorphous silicon active layer (index of refraction $n = 2.18$) enclosed between two distributed Bragg reflectors (DBR). Each DBR is composed of alternating $\lambda/4$ thick silicon oxide and silicon nitride layers with refractive indices 1.45 and 1.72, respectively.

The $m = 1$ cavity mode was tuned to the wavelength corresponding to the emission maximum of amorphous silicon active layer by choosing the appropriate value for λ and growing the layers accordingly. The PL spectrum of bulk amorphous silicon is shown in Fig. 3.2, and the maximum emission is at 715 nm. This yields geometrical layer thicknesses of 164 nm and 328 nm for the $\lambda/2$ and λ hydrogenated amorphous silicon active layers, respectively, and 123 nm and 104 nm for the silicon oxide and silicon nitride DBR layers, respectively.

The schematic and the scanning electron microscope (SEM) picture of one of our microcavity structures is shown in Fig. 3.1. The 328 nm thick hydrogenated amorphous silicon layer can be distinguished in the middle, although it is mixed up a little with the silicon oxide layers enclosing it. The dark regions are 104 nm thick silicon nitride layers, and the light gray regions are 123 nm thick silicon oxide layers.

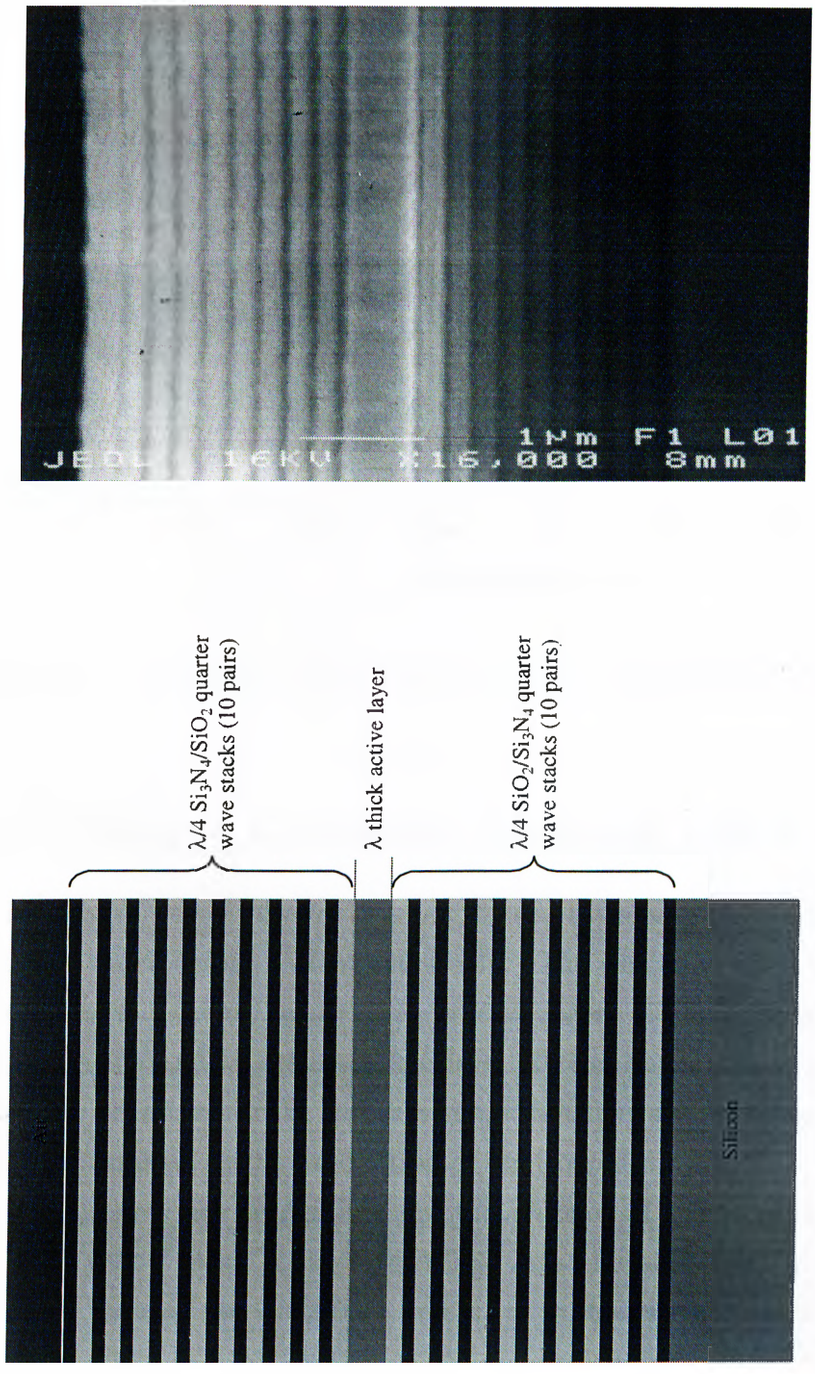

Figure 3.1: The planar microcavity structure with DBR mirrors

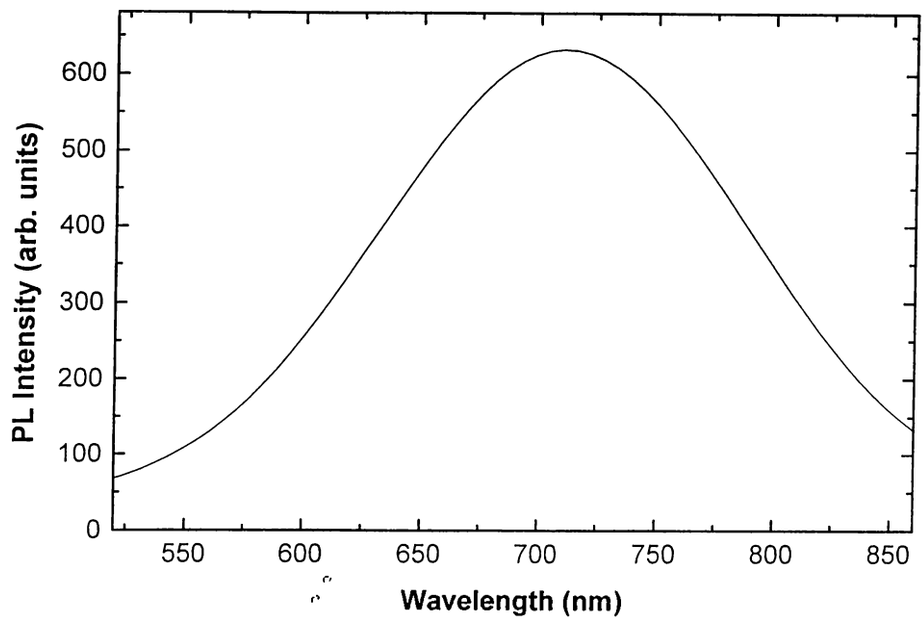

Figure 3.2: Photoluminescence spectrum of bulk hydrogenated amorphous silicon

3.2 Sample Cleavage, Cleaning and Cleanliness

In the field of device physics cleaning means to remove the undesired materials from the wafer before each process step. The dirt may come either from the surroundings or from the previous process steps. Cleanliness is to prevent the contamination and to maintain the level of cleanliness that is already present. These two definitions are in fact very simple but they are very crucial for achieving high performances in the production of semiconductor devices.

Clean rooms are categorized by the number of particles contained in the air. Our yellow clean room categorized as a class-100 clean room has 100 or less particles that are 0.5 μm or greater in diameter, in a cubic foot of air. A class-100, which is used for fabrication of semiconductor devices, requires good filtering techniques and protective clothing on personnel. Class-10,000, which is

relatively easy to obtain, is generally used for semiconductor characterization. For comparison this information has to be given: the general environment of an average building usually exceeds class 100,000.

Because we fabricate our devices in just one step by PECVD, cleaning operation is performed once, after cleaving. The wafers are cleaved into pieces of dimensions $1,5 \times 2\ cm^2$ to fit them into our reflectance measurement setup. This size is also big enough to assume in theoretical calculations that the cavity has infinite dimensions in the $x - y$ plane because samples are pumped with a focused laser beam whose size is $40 \times 1200\ \mu^2$ which is very small compared to that of samples'. Plasma etching, acids bases, and solvent cleaning are the basic cleaning methods. In our processes we performed 3-solvent cleaning, in which the solvents are Trichlorethan(TCE), Aceton(ACE), and Isopropyl Alcohol(ISO). The samples were boiled for 2 minutes in TCE , and then left at room temperature for 5 minutes in ACE bath. After that, they were boiled for 2 minutes in ISO and then rinsed with DI (de-ionized) water. Drying is very important such that no droplets should be evaporated on the surface since they carry dirt. For this reason nitrogen gun is used for removing the water from the surface. Finally the samples are kept on the hot plate at 120°C for 50 seconds. The solvents are semiconductor (SC) grade, that is they are extremely pure and filtered in sub-microns. Organic solvents are effective in removing oils, greases, waxes and organic materials. Many cleaning methods with various materials procedures do exist, and they are chosen by trial and error.

3.3 Plasma Enhanced Chemical Vapor Deposition (PECVD)

Plasma processing is used extensively in the semiconductor industry for etching and growth of thin film materials.[23] Plasma assisted techniques are especially important in deposition of thin-film materials because they can be accomplished at relatively low temperatures. Such materials could be deposited on wafers

using *chemical vapor deposition*, in which the reactant species are introduced into the vicinity of a hot wafer by gaseous flow and the appropriate reactions take place to grow the material on the wafer surface. The temperatures required to drive this chemical reactions are often 700° to 1000° C. For gallium arsenide wafers, arsenic evolves in this temperature range. Metals commonly present on the wafer can not be exposed to these extremes either. As one example ohmic constants are formed at approximately 450° C. Temperatures above 500° C will rapidly destroy the ohmic contact. Therefore CVD is not a generally useful technique, so low-temperature, plasma driven reactions are used instead. The plasma-assisted deposition process is denoted as *plasma-enhanced chemical vapor deposition* (PECVD).

PECVD yields films that are amorphous in nature with very little short-range structural ordering. Chemical bonding within the film may vary. The plasma-assisted deposition process sometimes has been called *plasma polymerization* to emphasize that the film may be randomly bonded, highly cross-linked, and of variable composition. Species reach the surface in a haphazard manner, and may be quickly covered and incorporated into the film. Therefore, chemical species other than the desired ones are often included in the film. In this sense, plasma-assisted deposition is more complex than plasma-assisted etching, in which it does not much matter what the final products are, because they disappear into the pumps.

From the perspective of a physicist, the plasma state encompasses a wide range of electron energies and densities and includes such phenomena as flames, low-pressure arcs, solar coronas, and thermonuclear reactions. The regime of interest to semiconductor processing is the low-pressure plasma or *glow discharge*. These plasmas are characterized by gas pressures on the order of 0.1 to several Torr, free-electron densities of 10^9 to 10^{12} cm^{-3}, and electron energies of 1 to 10 eV.

The plasma is able to generate chemically reactive species at relatively low temperature because of the nature of the plasma state. The temperature of the chemical species (atoms, molecules, or radicals), as represented by their translational and rotational energy, is generally near ambient. The electrons,

however, can exhibit temperatures of tens of thousands of degrees Kelvin. The electron energy is sufficient to break molecular bonds and create chemically active species in the plasma. Any of these species can be excited to higher electronic energy states by further interaction with the electrons. Hence, chemical reactions that usually occur only at high temperatures can be made to occur at low or even ambient temperatures in the presence of an activating plasma state. Most of the species remain neutral in glow discharges. This feature allows most of the plasma to remain near ambient temperatures. Although the ionization rate is small, it is adequate to provide sufficient number of reactive species. The light glow emitted from the plasma is characteristic of the electronic transitions taking place. The wafer is generally heated to aid the deposition process, but usually less than a few hundred degrees Celsius.

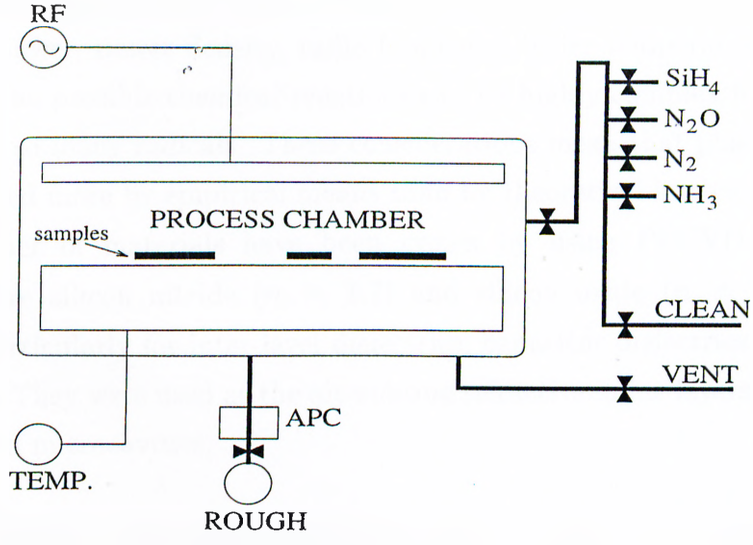

Figure 3.3: The PECVD system

Plasma processing occurs in equipment called *plasma reactors*. The one that we use is a planar-configured one (see Figure 3.3) which is capable of high uniformity. Wafers are placed on the lower electrode, which is also used to heat wafers. The 13.56 MHz RF signal which excites the plasma is applied across the two electrodes. The reactant gases are introduced at the outer radius, and flow radially between the electrodes. The plasma occupies the region between

the two electrodes, but is excluded from the immediate vicinity of the electrode surface by electromagnetic effects. This region is called the *plasma sheath* or the *dark region* (because it doesn't glow). It is on the order of 0.1 to 10 mm thick, depending on the operating conditions. The plasma is generally neutral, with positive species balancing negative ones. However; the plasma sheath is a region of positive space charge and the electrode surfaces are negative with respect to the plasma. This is due to the higher mobility of electrons which move rapidly to the surface of electrodes. The RF voltage is applied through a large blocking capacitor so that no dc bias is intentionally applied. Most of the voltage between the two electrodes is dropped across the two plasma sheaths.

The plethora of chemical species in the plasma and the nature of the plasma state make processing results extremely sensitive to virtually all possible parameters: gas type, gas flow rate, gas delivery position, pressure, electrode geometry, power, power density, radio frequency, wafer temperature, and wafer material. The possible chemical reactions can be highly complex because of the presence of so many radicals. These considerations mean that plasma processes are developed more by empirical means than by theoretical analysis.

A number of materials have been grown by using PECVD. The major materials are silicon nitride ($n = 1.7$) and silicon oxide ($n = 1.4$). These are used particularly for inter-level dielectrics, capacitor dielectrics, and scratch protection. They were used as the alternating refractive index layers of the DBRs of fabricated microcavities.

3.3.1 Silicon Nitride Deposition

A mixture of 2% silane (SiH_4) and 98% nitrogen (N_2) is used as the silicon source, and ammonia (NH_3) as the nitrogen source. The desired overall reaction would be

$$3SiH_4 + 4NH_3 \longrightarrow Si_3N_4 + 12H_2$$

or

$$3SiH_4 + 2N_2 \longrightarrow Si_3N_4 + 6H_2$$

but there are enormous number of possible intermediate reactions. The plasma conditions make the presence of SiH_4, SiH_3, SiH_2, NH_3, NH_2, and ionized hydrogen likely. Oxygen may be present from background gases or water. Carbon may be present from background hydrocarbons, such as pump oil. The resulting "silicon nitride" may include Si, N, O, H, and C. Even in the complete absence of background components or contamination, hydrogen will be included in the film because of ammonia. In fact, plasma Si_3N_4 can contain as much as 20-25% hydrogen.[8,12] So the Si/N ratio will not necessarily be 3/4, it is a function of the operating parameters.

The recipe in Table 3.1 was found by empirical means and used, to deposit approximately 1040Å thick Si_3N_4 layer.

Automatic Pressure Controller (APC) Pressure	1000 mTorr
RF Power	20 W
Temperature	100°C
2%SiH_4+98%N_2 Flow Rate	180 sccm
NH_3 Flow Rate	10 sccm
Process Time	5.60 minutes

Table 3.1: PECVD of silicon nitride recipe

3.3.2 Silicon Oxide Deposition

Although it is common to refer to plasma deposited silicon oxide as "silicon dioxide", the same caveats on stoichiometry that applied to silicon nitride also apply here: the Si/O ratio may depart from 1/2, and a certain amount of hydrogen will exist in the film.

A mixture of 2% silane (SiH_4) and 98% nitrogen (N_2) is used as the silicon source again, and nitrous oxide (N_2O) as the oxygen source. The desired overall reaction would be

$$SiH_4 + 2N_2O \longrightarrow SiO_2 + 2N_2 + 2H_2$$

Oxygen has a much greater affinity for reacting with silane than does nitrogen. Hence, silicon oxide formation dominates over silicon nitride formation. The recipe in Table 3.2 was used to deposit approximately 1230Å thick SiO_2 layer.

Automatic Pressure Controller (APC) Pressure	1000 mTorr
RF Power	20 W
Temperature	100°C
2%SiH_4+98%N_2 Flow Rate	180 sccm
N_2O Flow Rate	25 sccm
Process Time	2.81 minutes

Table 3.2: PECVD of silicon oxide recipe

The thickness and the refractive indices of silicon oxide and silicon nitride layers were measured by an AutoEL III ellipsometer. Although the precision of the ellipsometer is 1Å, subsequent measurements may differ, e.g. about 10-20Å for 1230Å thick silicon oxide layer, which means an error of about 1.5%.

3.3.3 Hydrogenated Amorphous Silicon Deposition

Hydrogen is included in the plasma deposited film because silane is used as the silicon source. Like "silicon nitride" and "silicon oxide", again, although we refer to our plasma deposited material as "hydrogenated amorphous silicon", it may contain N, because silane is mixed with a carrier gas, N_2. Oxygen may be present from background gases or water, carbon may be present from background hydrocarbons. So the resulting "hydrogenated amorphous silicon" may include Si, H, N, O, and C.

The recipe used to deposit approximately 1640Å thick hydrogenated amorphous silicon layer is given in Table 3.3.

Ellipsometer can not measure the thickness and the refractive index of amorphous silicon. The thickness was measured by a Veeco DEKTAK 3030 ST surface texture analysis system to be 1640 ± 30Å and the refractive index was estimated from the literature to be 2.18.[26,27]

Automatic Pressure Controller (APC) Pressure	1000 mTorr
RF Power	20 W
Temperature	100°C
2%SiH_4+98%N_2 Flow Rate	180 sccm
Process Time	6.34 minutes

Table 3.3: PECVD of hydrogenated amorphous silicon recipe

Chapter 4

Characterization and Results

After the fabrication processes, photoluminescence (PL) and reflectance spectra of microcavities were measured. The room temperature PL spectra were taken by a 1 meter Jobin-Yvon U1000 double-grating monochromator. The exit slit of the monochromator was equipped with a water cooled GaAs photomultiplier tube (PMT) and standard photon counting electronics. The room temperature reflectance measurements were made using a Varian Cary 5 spectrophotometer.

4.1 Photoluminescence Spectrum

PL study of a sample is a good technique to characterize the material, revealing the optical characteristics of the sample.[7] To investigate the emission properties of the sample, a PL spectrum is necessary. This analysis helps in understanding the energy band structure of the sample, therefore determining the emission wavelength, together with some other material parameters.

The interaction of light with semiconductors occur at the spectral range $0.1 - 1000\mu m$ $(0.001 - 12eV)$. In the near ultraviolet, visible, near infrared region $(0.24-3.1eV)$ the dominant effect is absorption at the band gap and by impurities, leading to PL under certain conditions.

A valence electron can be excited across the band gap of a semiconductor with an incoming photon, whose energy equals to or exceeds the gap value. Absorption

also occurs, when the photon raises an electron from a neutral donor to the conduction band, or from the valence band to a neutral acceptor. It is also possible to induce absorptive transition from the valence band to an ionized donor, or from an ionized acceptor to the conduction band. These processes lead to the sensitive probe of PL, which occurs when the excited electron returns to its initial state. This process can be either radiative or non-radiative. If it is radiative, it emits a photon whose energy gives the difference between the excited and the initial state energies. The emission spectrum shows a fingerprint peak related to the energy of each excited level.

The gap being direct or indirect strongly affects the absorption process. The incoming photon carries negligible momentum compared to that of the electron, so the absorbing electron gains energy without changing its wavevector. In a direct gap semiconductor like GaAs an electron at the valence band maximum, executes a vertical transition to the conduction band minimum directly above. From the energy conservation,

$$\hbar w = E_f - E_i \tag{4.1}$$

where E_f and E_i are the final and initial energies and $\hbar w$ is the photon energy.

For an indirect gap semiconductor like crystalline silicon, the excited electron needs additional momentum to reach the conduction band minimum at a nonzero wavevector. It gains this momentum with a phonon.

$$\hbar w = E_f - E_i \pm \hbar\Omega \tag{4.2}$$

where $\hbar\Omega$ is the phonon energy. $\pm$ corresponds to the phonon emission and absorption. Phonon emission dominates at low temperatures since there are less phonons. The need for an additional third body interaction with the phonon makes indirect absorption far less probable then direct absorption, meaning that the absorption is weaker.

After any of the absorption processes separates an electron and a hole, they recombine. This can proceed in either radiative or non-radiative form. In a direct

gap semiconductor, the recombination transition is vertical, and the emitted photon energy is given by Equation 4.1. For an indirect gap, a phonon must be involved as in indirect absorption, and the energy of the emitted photon is given by Equation 4.2.

Because of the same reason, as in absorption, the indirect process is much less probable than direct recombination. This explains why crystalline silicon, with its indirect band gap, is a poor luminescence emitter.

Although radiative emission is in many ways the inverse of absorption, there are two main distinctions. One is that recombination is a non-equilibrium process, requiring a supply of electrons at energies above their equilibrium values. For this reason lasers are used as pumping sources. Second, all electronic states whose energy difference obey the conservation law participate in absorption, leading to broad spectral features. But for emission, the recombining electron hole pairs have well defined energy levels, resulting in narrow spectral features. This is why PL is a better tool for characterization than absorption spectroscopy. The sharp peaks of PL can yield highly accurate values for the gap and impurity energies.

4.1.1 Experimental Method

The general PL arrangement is shown on Figure 4.1. The source can be any laser whose photon energy exceeds the bandgap of the material to be examined. In our experiments we used an Ar^+ laser with a wavelength of 514.5 nm (or 488 nm) which has a bigger energy than the light emitted by amorphous silicon in the cavity.

The laser beam with a power of 150 mW was focused by a 15 cm focal length cylindrical lens on the samples. The PL spectra were taken at $0 \pm 3.6°$ with the excitation laser at 30° with respect to the surface normal. Laser power can not be increased indefinitely, since too high an intensity at the focused spot can damage the sample. However, tens of milliwatts are often adequate to give good signals.

The PL signal, obtained by the laser impinging the sample, passes through a double grating monochromator which selects a wavelength to transmit to the

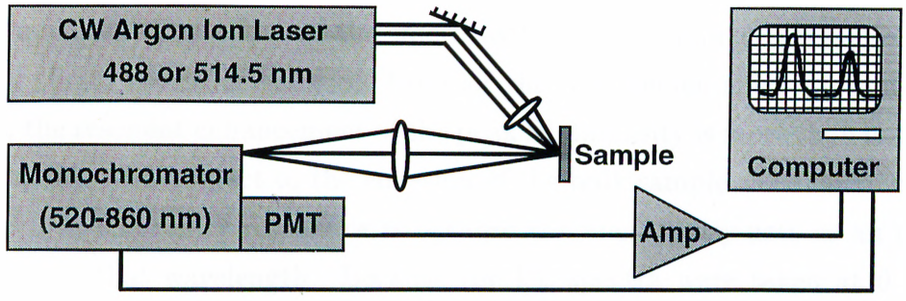

Figure 4.1: PL setup

detector. As the detector (photomultiplier tube) counts the number of photons, the PL spectrum of the sample, namely the intensity versus wavelength graph is obtained.

PL spectrum of a $\lambda/2$ thick microcavity enclosed between two DBRs which have 14 pairs of alternating silicon nitride and silicon oxide layers is shown in Fig. 4.2. PL spectrum of amorphous silicon multiplied by 10 is also plotted

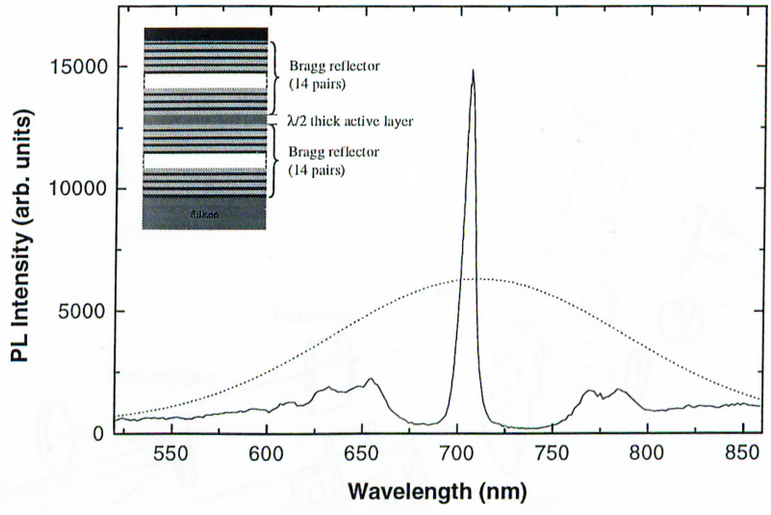

Figure 4.2: Photoluminescence spectrum of $\lambda/2$ thick microcavity with 14 pairs of DBR mirrors (solid line) and bulk amorphous silicon (dotted line). The data of the amorphous silicon were multiplied by 10 for comparison. The inset shows the schematic of the structure.

for comparison. The effect of the microcavity on the amorphous silicon PL is twofold: first, the wide emission band of the amorphous silicon is narrowed; second, the resonant enhancement of the peak PL intensity is more than one order of magnitude with respect to the emission of the bulk sample. The enhancement of the PL at the cavity resonance is because the microcavity acts as an optical resonator at that wavelength. Because the PL spectra were taken at $0 \pm 3.6°$ with respect to the surface normal, this enhancement is partly because of the highly directional emission pattern of the cavity (See Figure 2.6 for the calculated pattern). The SE lifetime change, which is calculated to be shorter by a factor 2/3 in Chapter 2, may be another reason. However, a real proof of the SE lifetime change requires measurements of the SE lifetime in the time domain.[20]

4.2 Reflectance Measurements

The room temperature reflectance measurements were made by a Varian Cary 5 spectrophotometer. The optical design of the spectrophotometer is shown in

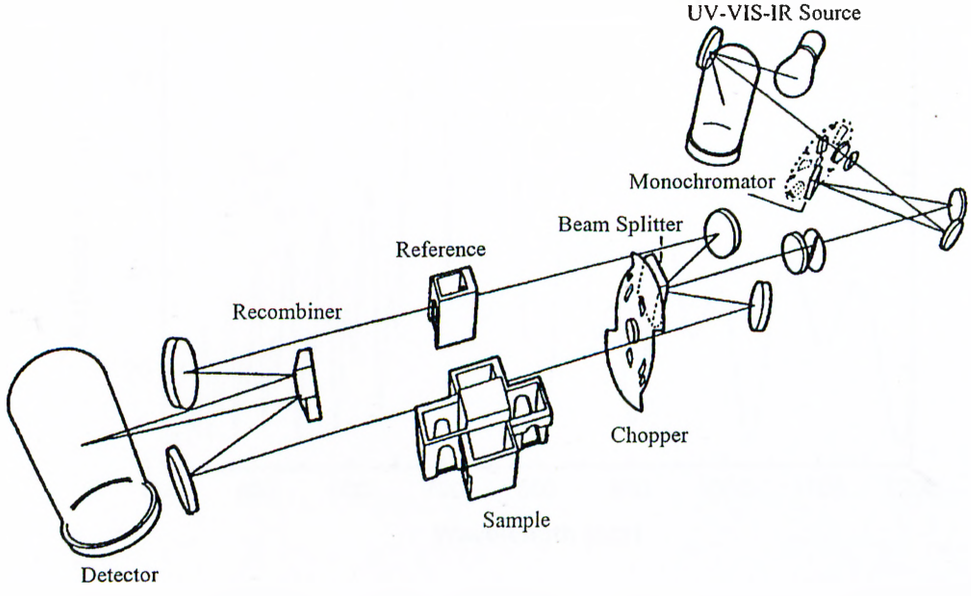

Figure 4.3: The optical design of the reflectance setup

Fig. 4.3.[28] The light from the source which passes through the filter wheel is directed through the entrance slit into the monochromator, where the grating disperses the light into its monochromatic components. After passing the monochromator, the light is split into two equal beams. One of the beams is directed onto the sample at 0° with respect to the surface normal and reflected, the other is used as reference beam to compensate the spectrum obtained for changes in some of the system variables. The beams are then recombined and enter the detector compartment. Reflected intensity is measured relative to a "perfect reflector", which was an aluminum mirror.

Reflectance vs. wavelength and frequency spectrum of a $\lambda/2$ thick microcavity enclosed between two DBRs which have 10 pairs of alternating silicon nitride and silicon oxide layers is shown in Figs. 4.4 and 4.5, respectively.

Reflectance vs. frequency spectrum looks symmetrical because the adjacent reflection minima and maxima are equally spaced in frequency scale.

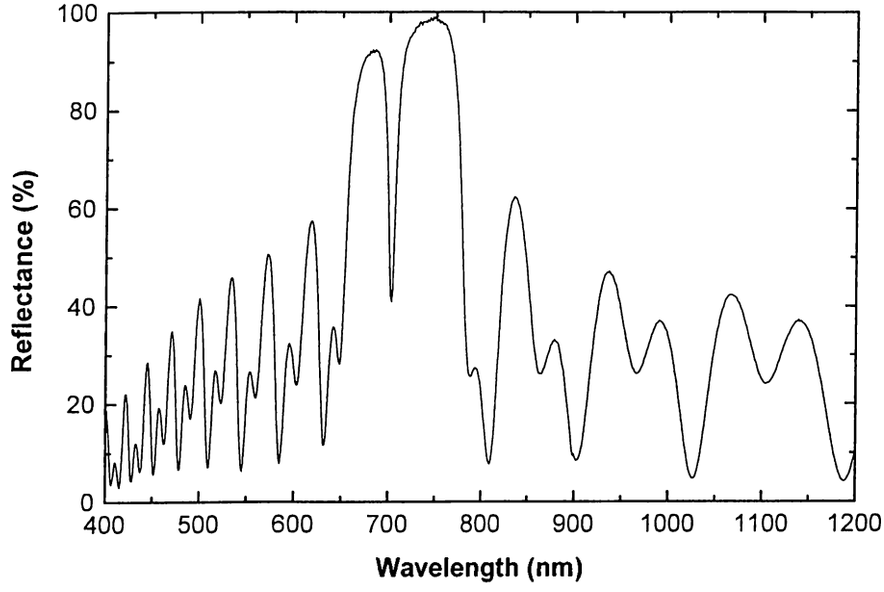

Figure 4.4: Reflectance vs. wavelength spectrum of $\lambda/2$ thick microcavity with 10 pairs of DBR mirrors

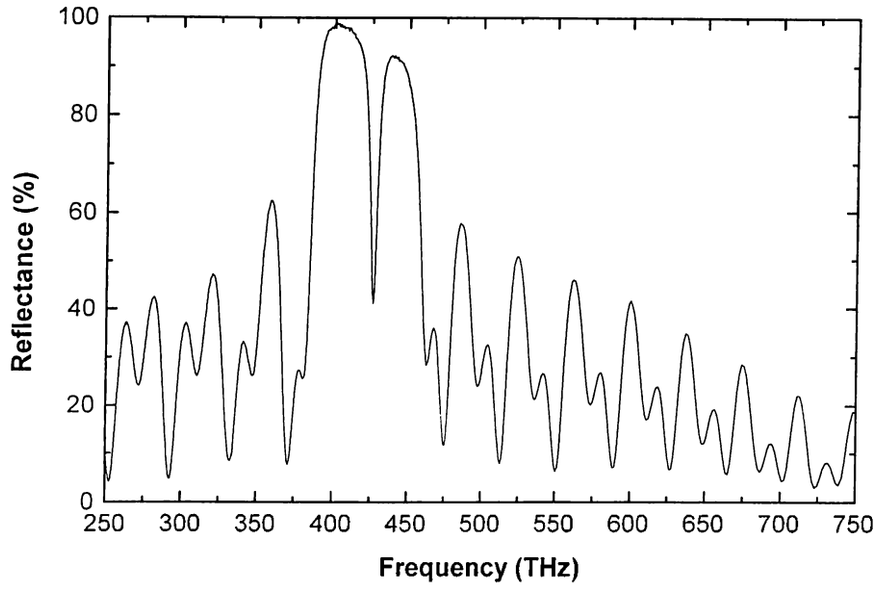

Figure 4.5: Reflectance vs. frequency spectrum of $\lambda/2$ thick microcavity with 10 pairs of DBR mirrors

4.3 Microcavity Results

Experimental and calculated reflectance spectra of a DBR which has 10 pairs of alternating silicon oxide and silicon nitride layers is shown in Fig. 4.6. The DBR is highly reflective over a range of 80 nm (stopband of the cavity transmission) centered at 715 nm and the maximum reflection is 96%.

Calculations are done by TMM, as explained in the 'Analysis of Multilayer Thin Films' section in Chapter 2.

Experimental and calculated reflectance spectra of a $\lambda/2$ thick microcavity with 10 pairs of DBR mirrors is shown in Fig. 4.7. Cavity resonance wavelength is 707 nm, which is the position of the dip in the stopband. Assuming that the measured thickness of the active layer was correct, the best match with the experimental spectrum was obtained when the refractive index of the active amorphous silicon layer was taken to be 2.03. The value 2.18 for the amorphous

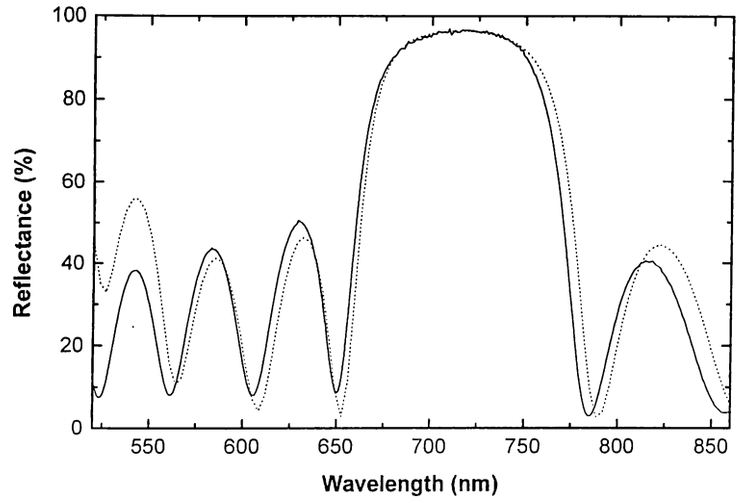

Figure 4.6: Experimental (solid line) and calculated (dotted line) reflectance spectra of a DBR which has 10 pairs of alternating silicon oxide and silicon nitride layers.

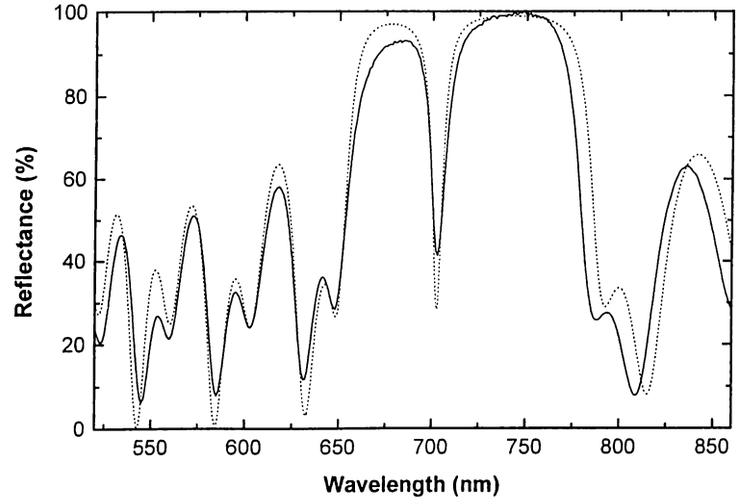

Figure 4.7: Experimental (solid line) and calculated (dotted line) reflectance spectra of $\lambda/2$ thick microcavity with 10 pairs of DBR mirrors.

silicon's refractive index was found from the literature and used when determining the thickness of the active layer. This also explains the shift in the cavity resonance wavelength, which would coincide with the center of the stopband if the refractive index of the amorphous silicon was 2.18.

Figure 4.8 shows the reflectance and photoluminescence spectra of $\lambda/2$ thick microcavity with 14 pairs of DBR mirrors. The PL peak and the dip of the reflectance spectrum coincide at 707 nm. The resonant transmission bandwidth is 5 nm. PL peak has a full width at half maximum of 7 nm. During the PL measurements, the temperature of the sample was not controlled, so there could be local heating owing to the poor thermal conductivity of the substrates which reduces the PL efficiency and broadens the PL linewidth.

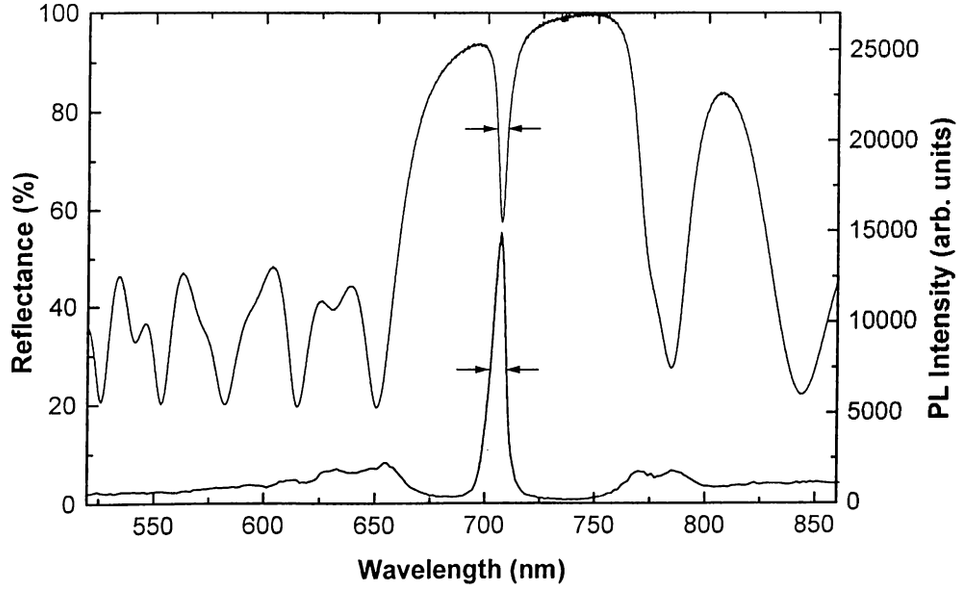

Figure 4.8: Reflectance and PL spectra of $\lambda/2$ thick microcavity with 14 pairs of DBR mirrors.

The quality factor Q of the cavity can be calculated by using Eq. 2.21

$$Q = \frac{\lambda_0}{\delta\lambda} = \frac{707}{5} = 141.$$

Q was estimated to be 313 for a microcavity with 14 pairs of DBR mirrors, but that was calculated by taking the reflectances of the mirrors as 99.1% (See "Microcavity Analysis" section in Chapter 2), which is the reflectance maximum of the DBRs. However the fabricated structure's cavity resonance is at 707 nm, where the reflectivity is 98%. Using Eq. 2.75 this gives a quality factor of 155 which is close to the experimental value 141.

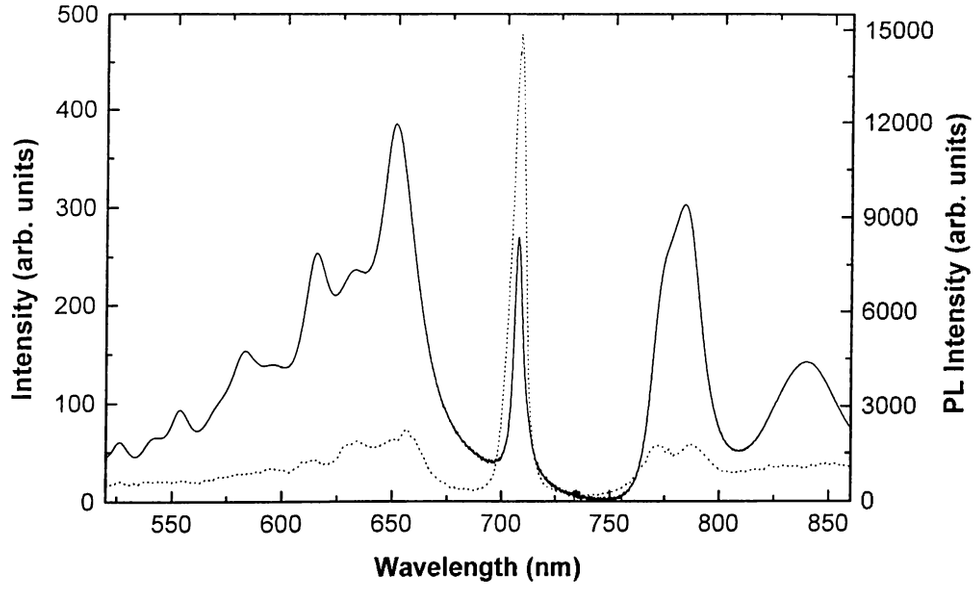

Figure 4.9: Modeled emission (solid line) and PL (dotted line) spectra of $\lambda/2$ thick microcavity with 14 pairs of DBR mirrors

In order to prove that the microcavity structure does not act to simply filter the spontaneous emission, which would yield only a relative and not an absolute enhancement, the emission spectrum of $\lambda/2$ thick microcavity with 14 pairs of DBR mirrors was modeled as the photoluminescence spectrum of the bulk amorphous silicon multiplied by the transmission spectrum of the sample. The spectral shapes of PL can not be reproduced (See Fig. 4.9) by simply multiplying the PL spectrum of the bulk by the transmittance of the sample.

4.3.1 Effect of the Top Mirror

To permit the light escape from the cavity, a partially transmitting mirror is often used as one of the mirrors. To investigate the effect of the top mirror reflectance on the PL intensity and the reflectance spectrum, three $\lambda/2$ thick microcavity with 10 pairs of bottom DBRs, and 10, 9.5, and 9 pairs of top DBRs were fabricated and labeled A, B, and C respectively. Three substrates were put in the plasma chamber and common parts, the bottom mirror and the active layer, are deposited on the substrates. Then the chamber was opened and three more substrates, labeled D, E, and F were put for deposition of only top mirrors of structures A, B, and C. After depositing 9 pairs of DBR layers, C and F were taken out, one more layer of silicon oxide was deposited and B and E were taken out, and after the deposition of one more layer of silicon nitride process was over.

The reflectance and photoluminescence spectra of structures A, B, and C are shown in Fig. 4.10 and Fig. 4.11, respectively. Reflectances at the cavity resonance wavelength are 41%, 7.9%, and 30.5%, resonant transmission bandwidths are 10 nm, 11.8 nm, and 10.5 nm, and emission maxima are 12912, 15072 and 13950 for structures A, B, and C respectively.

Light coupling out of the cavity is best achieved in structure B (the one which has the highest emission maximum and lowest reflectance at the cavity resonance wavelength). The reason behind that is the top mirror of B, structure E, has the highest transmittance (10.7%, See Fig. 4.12). However, the higher the transmission of the top mirror, the higher the loss. That's why B has the broadest resonant transmission bandwidth.

Although F has 9 pairs of layers, which is one less than E's, its reflectance is higher. The only other difference between them is that F ends with a silicon nitride layer, and E with a silicon oxide layer. Therefore, the reason must be the refractive index difference; because the refractive index difference at silicon nitride-air interface is higher than silicon oxide-air interface's index difference, reflectance of F is higher than that of E. As a result F has a lower emission maxima and narrower resonant transmission bandwidth.

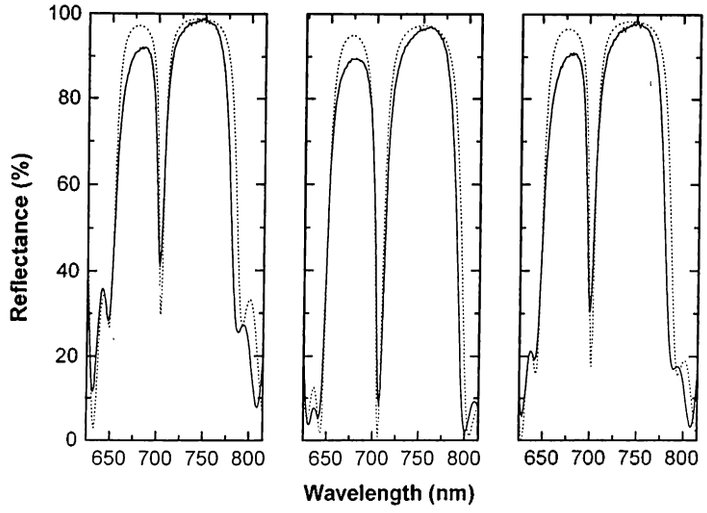

Figure 4.10: Experimental (solid line) and theoretical (dotted line) reflectance spectra of structures A, B, and C respectively. Structure A has a top mirror of 10 pairs, B 9.5 pairs, and C 9 pairs. Reflectances at the cavity resonance wavelength are 41%, 7.9%, and 30.5% respectively.

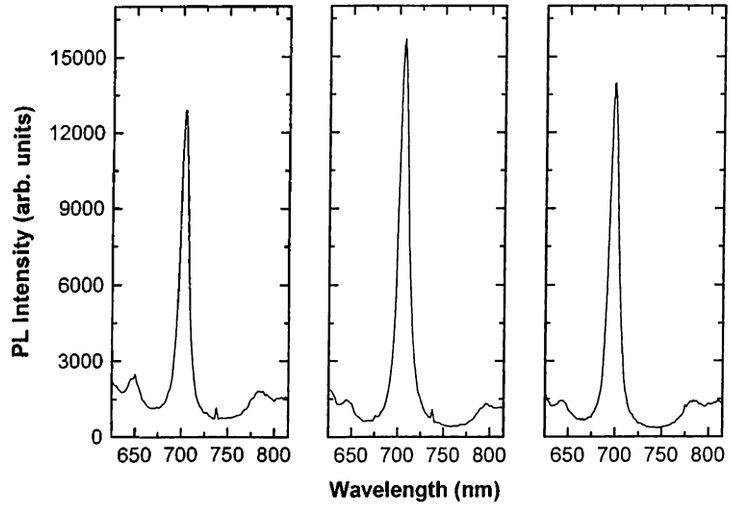

Figure 4.11: PL spectra of structures A, B, and C respectively. A, B and C have emission maxima of 12912, 15072 and 13950 respectively.

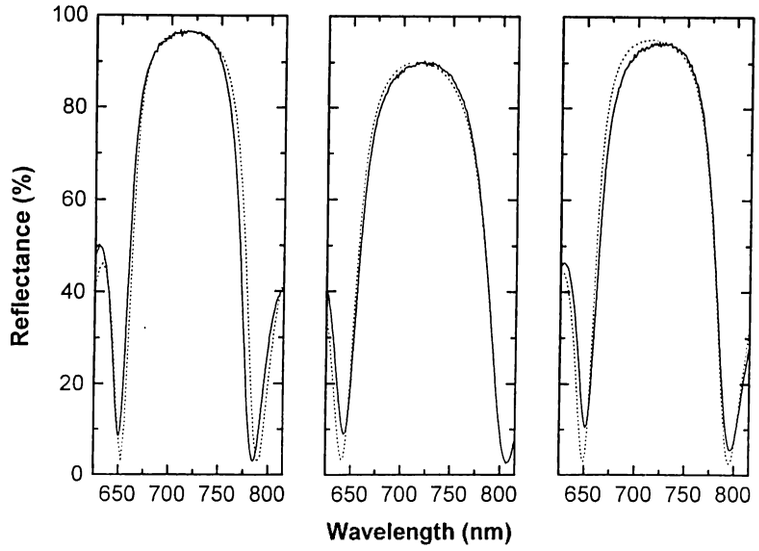

Figure 4.12: Experimental (solid line) and theoretical (dotted line) reflectance spectra of top mirrors D, E, and F respectively. D is the top mirror of structure A, E is B's, and F is C's. Reflectance maxima are 96%, 89.3%, and 93.7 respectively.

4.3.2 λ Thick Microcavity

The thickness of the resonator, $d = m\lambda/2n$, must be an integer multiple of half wavelengths in order resonance to occur. A structure with λ thick active layer with 10 pairs of DBRs was fabricated, and its optical response is compared to the $\lambda/2$ thick cavity which also has 10 pairs of DBRs. Figure 4.13 and Figure 4.14 shows the reflectance and photoluminescence spectra of $\lambda/2$ thick and λ thick structures, respectively. As it is seen in the figures there is not a significant difference between the two types, the same cavity effects are observed in the λ thick cavity too. The stronger emission of the λ thick cavity is related to the larger active thickness.

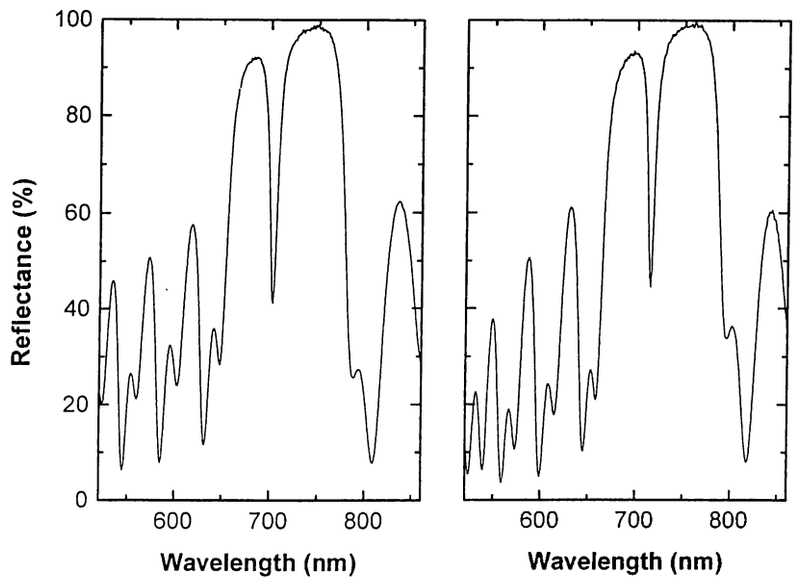

Figure 4.13: Reflectance spectra of $\lambda/2$ and λ thick cavities.

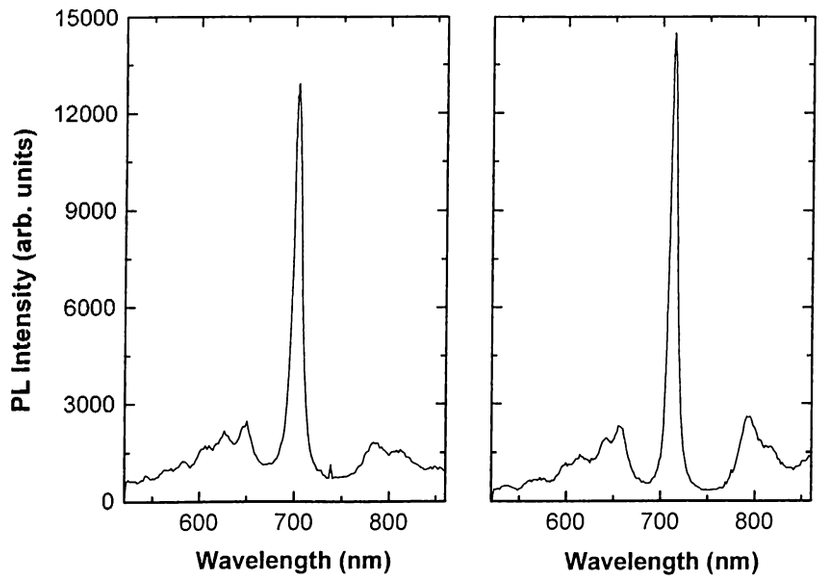

Figure 4.14: PL spectra of $\lambda/2$ and λ thick cavities.

4.3.3 The order of DBR Layers

The DBRs of the cavities are formed by periodic alternating silicon nitride and silicon oxide layers symmetric about the active layer. But there may be two different symmetrical configurations; active layer may be enclosed by silicon oxide layers, or silicon nitride layers. To investigate the effects of these configurations, two $\lambda/2$ thick microcavities with 7 pairs of DBR layers were fabricated. The only difference is that in one, active layer was enclosed by two silicon nitride layers, and in the other by two silicon oxide layers. If **L** and **H** stand for low (silicon oxide) and high (silicon nitride) refractive index layers, the structures can be written as $Si(\mathbf{LH})^7a - Si(\mathbf{HL})^7Air$ and $Si(\mathbf{HL})^7a - Si(\mathbf{LH})^7Air$.

Experimental and theoretical reflectance and the photoluminescence spectra of the two structures are shown in Figures 4.15, 4.16, and 4.17 respectively. Resonant transmission bandwidth and the PL FWHM of the structure $Si(\mathbf{HL})^7a - Si(\mathbf{LH})^7Air$ are about 10 nm wider than others, and the emission maximum is 1.85 times smaller.

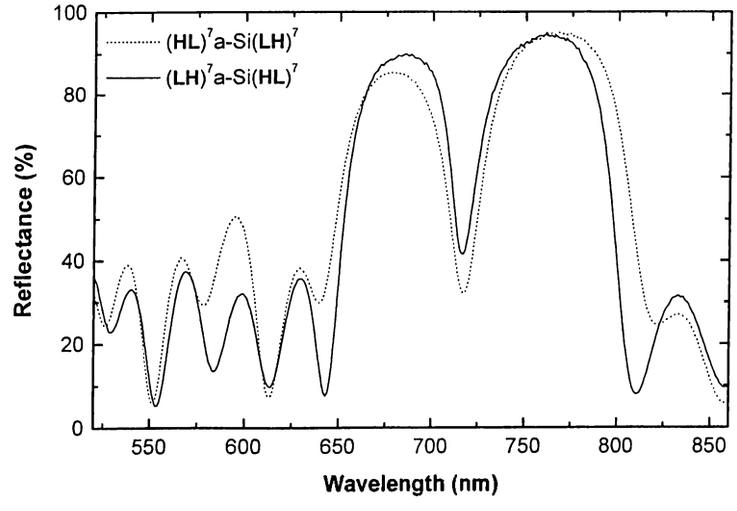

Figure 4.15: Experimental reflectance spectra of structures $Si(\mathbf{HL})^7a - Si(\mathbf{LH})^7Air$ and $Si(\mathbf{LH})^7a - Si(\mathbf{HL})^7Air$. **L** and **H** stand for low (SiO_2) and high (Si_3N_4) refractive index layers.

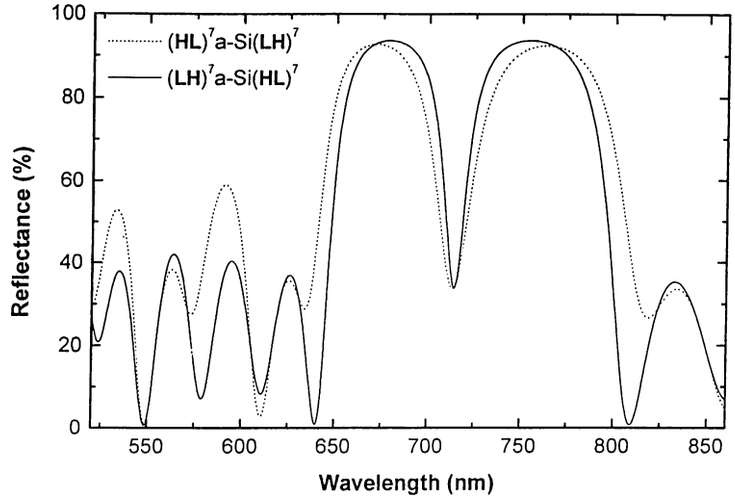

Figure 4.16: Theoretical reflectance spectra of structures $Si(\mathbf{HL})^7a-Si(\mathbf{LH})^7Air$ and $Si(\mathbf{LH})^7a - Si(\mathbf{HL})^7Air$.

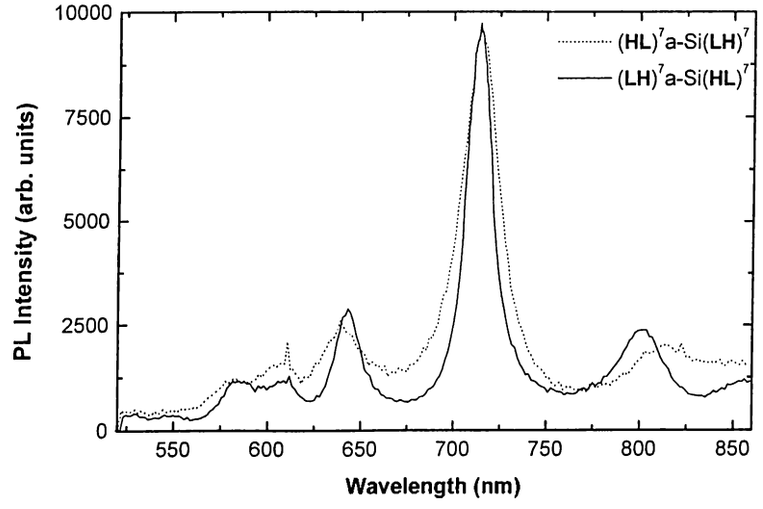

Figure 4.17: PL spectra of structures $Si(\mathbf{HL})^7a - Si(\mathbf{LH})^7Air$ and $Si(\mathbf{LH})^7a - Si(\mathbf{HL})^7Air$. Emission maxima are 5190 and 9600, respectively. The data of the structure $Si(\mathbf{HL})^7a - Si(\mathbf{LH})^7Air$ (dashed line) were multiplied by 1.85 for comparison.

Chapter 5

Conclusions

Amorphous silicon planar microcavities grown on Si wafers have been realized, thus the possibility of realizing versatile Si-based light emitting devices was explored. The microcavities consist of an active amorphous silicon layer sandwiched between two distributed Bragg reflectors. Stopband widths of 80 nm and 99% reflection at the middle of the stopbands were obtained by using alternating $\lambda/4$ thick silicon oxide and silicon nitride layers. The microcavity mode was tuned to the emission maximum of amorphous silicon (715 nm). Reflectance and photoluminescence (PL) measurements show cavity effects. Active layer emission was enhanced and the emission bandwidth was narrowed ($\delta\lambda = 7$ nm) noticeably in the PL spectra owing to the cavity induced modifications of the photon modes. Quality factors as high as 141 was obtained.

The reflectance spectra were simulated by the transfer matrix method. Excellent agreement between the theoretical and experimental spectra was obtained.

The effect of the number of top mirror layer pairs on the emission maximum and the transmittance at the cavity resonance was investigated both theoretically and experimentally. The reflectance of the DBR decreases as the number of layer pairs in the dielectric stack decreases. This, in turn, increases the emission maximum and the transmittance at the cavity resonance, because of increased light coupling out of the cavity.

A microcavity with a λ thick active layer was also fabricated and the same cavity effects were demonstrated.

Finally, the effect of the order of the DBR layers was investigated. The structure in which the active amorphous silicon layer is enclosed by two silicon nitride layers is concluded to give a narrower emission bandwidth, and a higher emission maximum.

Bibliography

[1] Y. Yamamoto and R. E. Slusher, "Optical Processes in Microcavities", Phys. Today, **46**, p. 66 (1993)

[2] R. E. Slusher and C. Weisbuch, "Optical Microcavities in Condensed Matter Systems", Solid Statem Commun., **92**, p. 149 (1994)

[3] EMIS group, "Properties of Amorphous Silicon", EMIS Datareviews Series No. 1, London: The Institution of Electrical Engineers (1989)

[4] P. Shaoqi and D. Xiaoning, "Properties of Sputtered Amorphous Silicon without Hydrogen", in H. Fritzsche, D. Han, C. C. Tsai (ed.s), *Proceedings of the International Workshop on Amorphous Semiconductors*, Singapore: World Scientific (1987)

[5] J. I. Pankove, "Luminescence in Hydrogenated Amorphous Silicon", in H. Fritzsche, D. Han, C. C. Tsai (ed.s), *Proceedings of the International Workshop on Amorphous Semiconductors*, Singapore: World Scientific (1987)

[6] J. D. Joannopoulos, and G. Lucovsky, "The Physics of Hydrogenated Amorphous Silicon", Berlin: Springer-Verlag (1984)

[7] S. Perkowitz, "Optical Characterization of Semiconductors", London: Academic Press (1993), p. 27

[8] W. A. Lanford, and M. J. Rand, J. Appl. Phys., **49**, p. 2473 (1978)

[9] K. H. Drexhage, *Progress in Optics*, Vol. 12, E. Wolf (ed.), North-Holland, New York (1974), p. 165

[10] Y. Yamamoto, G. Björk, H. Heitmann, and R. Horowicz, "Controlled Spontaneous Emission in Quantum Well Microcavities", in F. Henneberg, S. Schmitt-Rink, E. O. Göbel (ed.s), *Optics of Semiconductor Nanostructures*, Berlin: Akademie Verlag (1993)

[11] Y. Yamamoto, S. Machida, K. Igeta, G. Björk, "Controlled Spontaneous Emission in Microcavity Semiconductor Lasers", in Y. Yamamoto (ed.), *Coherence, Amplification, and Quantum Effects in Semiconductor Lasers*, Wiley Series in Pure and Applied Optics, USA: John Wiley and Sons, Inc. (1991)

[12] A. Aydınlı, A. Serpengüzel and D. Vardar, "Visible Photoluminescence from Low Temperature Deposited Hydrogenated Amorphous Silicon Nitride", Solid State Commun., **98**, 4 (1996)

[13] S. D. Bronson, and P. M. W. Skovgaard, "Optical Mode Density and Spontaneous Emission in Microcavities", in R. K. Chang, and A. J. Campillo (ed.s), *Optical Processes in Microcavities*, Advanced Series in Applied Physics, Vol. 3, Singapore: World Scientific (1996)

[14] B. E. A. Saleh and M. C. Teich, "Fundamentals of Photonics", USA: John Wiley and Sons, Inc. (1991)

[15] L. Levi, "Applied Optics", A Guide to Optical System Design, Vol. 2, USA: John Wiley and Sons, Inc. (1980), p. 47,67

[16] G. Björk and O. Nilsson, "A New Exact and Efficient Numerical Matrix Theory of Complicated Laser Structures: Properties of Asymmetric Phase-Shifted DFB Lasers", IEEE J. of Lightwave Technol. **LT-5**, 140 (1987)

[17] M. Born and E. Wolf, "Principles of Optics", Cambridge: Cambridge University Press (1998), p. 51

[18] M. Bass, E. W. Stryland, D. R. Williams, W. L. Wolfe (ed.s.), "Handbook of Optics", USA: McGraw-Hill, Inc. (1995), p. 42.38

[19] A.E. Siegman, "Lasers", University Science Books (1986)

[20] F. De Martini, G. Innocenti, G.R Jacobovitz and P. Mataloni, "Anomalous Spontaneous Emission Time in a Microscopic Optical Cavity", Phys. Rev. Lett. **59**, 2955 (1987)

[21] E. M. Purcell, "Spontaneous Emission Probabilities at Radio Frequencies", Phys. Rev. **69**, 681 (1946)

[22] K. Tanaka, T. Nakamura, W. Takamatsu, M. Yamanishi, Y. Lee and T. Ishihara, "Cavity Induced Changes of Spontaneous Emission Lifetime in One-Dimensional Semiconductor Microcavities", Phys. Rev. Lett. **74**, 3380 (1995)

[23] R. Williams, "Modern GaAs Processing Methods", Boston: Artech House, Inc. (1990), p. 153

[24] F. Tassone, C. Piermarocchi, V. Savona, and A. Quattropani, "Photoluminescence Decay Times in Strong-coupling Semiconductor Microcavities", Phys. Rev. B **53**, R7642 (1996)

[25] Y. Yamamoto, S. Machida, and G. Björk, "Microcavity Semiconductor Laser with Enhanced Spontaneous Emission", Phys. Rev. A **44**, 657 (1991)

[26] A. Serpengüzel, A. Aydınlı, and Alpan Bek, "Enhancement and Inhibition of Photoluminescence in Hydrogenated Amorphous Silicon Nitride Microcavities", Optics Express, **1**, No. 5, p. 108 (1997)

[27] A. Serpengüzel, A. Aydınlı, and Alpan Bek, "Alteration of Spontaneous Emission in hydrogenated Amorphous Silicon Microcavities", Journal of Non-Crystalline Solids, 227-230 (1998) 1142-1145

[28] B. J. Clark, T. Frost, M. A. Russel, "UV Spectroscopy Techniques, Instrumentation, Data Handling", Techniques in Visible and Ultraviolet Spectrometry Vol. 4, London: Chapman & Hall (1993)